1

Modeling: Understanding Metal-Nanoparticle Plasmons

The goal of this chapter is to provide a fundamental theoretical understanding of metal-nanoparticle plasmonics, and to introduce some of the analytical and computational approaches used to develop this understanding. We begin first with a brief review of the basics needed to understand light fields coupled with materials: Maxwell's equations, boundary conditions, the wave equation, dispersion relations, and dielectric response. Then, we begin a journey through increasingly confined metal strucutures. We start with bulk metals because that allows us to introduce the concept of plasmon excitations, describe the simple Drude model for metals, and discuss the dielectric response of real metals. Next, we consider a bulk metal terminated with a surface. This allows us to introduce the concept of surface plasmons: electron waves that propagate along the surface, coupled to fields that rapidly decay away from the surface. The strong localization of the excitation at the surface extends to metal nanowires, which can be thought of as metal surfaces rolled up upon themselves. The additional confinement in nanowires leads to discrete plasmon modes across the cross-section of the wires. Finally, we come to metal nanoparticles, where plasmons are confined in all three dimensions, leading to strong resonances at particular frequencies. With this foundation, we then discuss the optical response of metal nanoparticles, both in the near field and in the far field. Finally, we end this chapter by briefly touching on the behavior of the smallest metal particles, which can no longer be completely described by Maxwell's equations and classical dielectric response.

Understanding metal plasmonics can proceed from two different points of view. A microscopic, quantum-mechanical description identifies plasmons as collective

Introduction to Metal-Nanoparticle Plasmonics, First Edition. Matthew Pelton and Garnett Bryant.

excitations of the conduction electrons in the metal. In this picture, plasmons are charge-density waves that oscillate against the background of positive charge provided by atomic cores in the metal [1–4]. In this description, plasmon are damped by electron–hole pair excitations in the Fermi sea of conduction electrons (known as Landau damping). A microscopic picture is easiest to develop for bulk systems, where translational symmetry simplifies the many-body theory, or in small metal clusters with only a few conduction electrons.

Metal nanoparticles are, typically, too big to allow their properties to be calculated directly using a quantum-mechanical model, and do not have the translation symmetry that would simplify a many-body theory. However, a classical, macroscopic description has proven to provide an accurate and intuitive understanding of plasmon excitations in metal nanoparticles, even for nanoparticles with dimensions as small as a few nanometers. In the classical picture, plasmonic response is described as a local polarization of the metal particle induced by external driving fields. Once the macroscopic dielectric response of the metal is known, it can be used, together with Maxwell's equations, to determine the plasmon modes and optical response of the metal nanoparticles. The classical approach breaks down only if one does not have a good description of the dielectric response or if the particle size is comparable to the length scale for the onset of quantum effects (i.e., the Fermi wavelength, typically a few nanometers in noble metals).

This book therefore relies almost exclusively on the classical approach to modeling metal-nanoparticle plasmonics. This approach is the basis of nearly all the understanding of plasmons that has been developed; likewise, nearly all of the applications of metal-nanoparticle plasmons that are under investigation are based on their response to classical optical fields. In this approach, the presence of surfaces and the dimensionality and shape of a metal nanostructure plays a critical role in defining the optical response, but atomic-scale details do not matter. Classical models are all based on solving Maxwell's equations, subject to appropriate boundary conditions. We therefore begin by reviewing the basics of classical electrodynamics.

1.1 CLASSICAL PICTURE: SOLUTIONS OF MAXWELL'S EQUATIONS

1.1.1 Review of Classical Electrodynamics

A classical description of the interaction between light and a metal nanoparticle starts with a solution of Maxwell's equations. In Gaussian units, these equations are [5]

$$\nabla \cdot \mathbf{D} = 4\pi\rho\,, \tag{1.1}$$

$$\nabla \times \mathbf{E} = -\frac{1}{c}\frac{\partial \mathbf{B}}{\partial t}\,, \tag{1.2}$$

$$\nabla \cdot \mathbf{B} = 0\,, \tag{1.3}$$

$$\nabla \times \mathbf{H} = \frac{4\pi}{c}\mathbf{J} + \frac{1}{c}\frac{\partial \mathbf{D}}{\partial t}\,, \tag{1.4}$$

where ρ is the free charge density, $\mathbf{J}$ is the free current density, and c is the speed of light. The displacement field, $\mathbf{D}$, responds to free charges. It is related to the total electric field, $\mathbf{E}$, which includes the polarization fields of the materials, through a constitutive relation. For an isotropic material, the constitutive relation is simply

$$\mathbf{D} = \epsilon \mathbf{E}\,, \tag{1.5}$$

where ϵ is known as the dielectric constant. A similar constitutive relation connects the magnetic induction $\mathbf{B}$ and magnetic field $\mathbf{H}$: $\mathbf{B} = \mu \mathbf{H}$. At optical frequencies, all naturally occurring materials are nonmagnetic, so the magnetic permeability $\mu = 1$. (In Section 7.6.1, we discuss the possibility of producing artificial materials that effectively have $\mu \neq 1$.) In these equations, all fields are implicitly taken to be functions of time, t.

Maxwell's equations can be combined to give

$$\nabla^2 \mathbf{E} - \nabla(\nabla \cdot \mathbf{E}) = \frac{\epsilon}{c^2} \frac{\partial^2 \mathbf{E}}{\partial t^2}. \tag{1.6}$$

In the absence of any sources, $\nabla \cdot \mathbf{E} = 0$, and we obtain the following wave equation:

$$\nabla^2 \mathbf{E} = \frac{\epsilon}{c^2} \frac{\partial^2 \mathbf{E}}{\partial t^2}. \tag{1.7}$$

At any boundary, the components of $\mathbf{D}$ and $\mathbf{B}$ normal to the interface must be continuous. In addition, the components of $\mathbf{E}$ and $\mathbf{H}$ tangential to the interface must be continuous. Determining the response of an object to an applied electromagnetic wave is a matter of solving the wave equation, supplemented with the appropriate constitutive relations, subject to these boundary conditions.

Any solution can be written as a superposition of monochromatic plane waves, of the form $\mathbf{E} = \mathrm{Re}\left[\mathbf{E}(\omega) \exp(\imath(\mathbf{k} \cdot \mathbf{r} - \omega t))\right]$. For such a plane wave, we can immediately determine the dispersion relation that connects the wavevector $\mathbf{k}$ and the frequency ω:

$$\mathbf{k}^2 = \frac{\epsilon \omega^2}{c^2}. \tag{1.8}$$

This dispersion relation defines the character of solutions to the wave equation and determines how waves connect at interfaces. Waves are propagating if $\epsilon > 0$ and are evanescent if $\epsilon < 0$. Waves can be transmitted into a medium if $\epsilon_{\mathrm{med}} > 0$, and are reflected at the interface if $\epsilon_{\mathrm{med}} < 0$. For plane waves, Equation 1.1 gives $\mathbf{k} \cdot \mathbf{E} = 0$, so the polarization direction is perpendicular to the propagation direction. From Equation 1.2, $\mathbf{B} = (c/\omega)(\mathbf{k} \times \mathbf{E})$, so $\mathbf{B}$, $\mathbf{E}$, and $\mathbf{k}$ are mutually orthogonal and $|\mathbf{B}| = \sqrt{\mu/\epsilon}|\mathbf{E}|$.

Another key concept is the energy stored in the field, which is described by the energy density of the field and energy flow associated with the field. The energy density of the field, U, at any point is

$$U = \frac{1}{8\pi}(\mathbf{E}\cdot\mathbf{D} + \mathbf{B}\cdot\mathbf{H}). \tag{1.9}$$

The energy flow associated with the field, $\mathbf{S}$, also known as the Poynting vector, is

$$\mathbf{S} = \frac{c}{4\pi}(\mathbf{E}\times\mathbf{H}). \tag{1.10}$$

For monochromatic light with frequency ω, the energy density, averaged over one period, takes the simpler form

$$U = \frac{1}{16\pi}\mathrm{Re}\left[\epsilon\mathbf{E}\mathbf{E}^* + \mu\mathbf{B}\mathbf{B}^*\right]. \tag{1.11}$$

Similarly, the time-averaged Poynting vector is

$$\mathbf{S} = \frac{c}{8\pi}\mathrm{Re}\left[\mathbf{E}\times\mathbf{H}^*\right]. \tag{1.12}$$

U and $\mathbf{S}$ are connected by a conservation law that relates the change in energy density to energy flow and any work done on a current $\mathbf{J}$ interacting with the field:

$$\frac{\partial U}{\partial t} + \nabla\cdot\mathbf{S} = -\mathbf{J}\cdot\mathbf{E}. \tag{1.13}$$

For plane waves in a medium with constant ϵ, one can show that $U = (\epsilon/8\pi)|\mathbf{E}|^2$ and $\mathbf{S} = v_\phi U\hat{\mathbf{k}}$, where the phase velocity $v_\phi = c/\sqrt{\mu\epsilon}$. The energy flow is in the direction of propagation. The intensity, I, of the energy flow is the energy density times the speed of light in the medium.

Writing the solution to Maxwell's equations as a superposition of monochromatic waves makes it possible to take into account the finite response time of the material to the applied wave. In Equation 1.5, ϵ has been written as a constant, which implies that the displacement field responds instantaneously to the applied electric field. All real materials have a finite response time, however, that can be treated by writing the solution to Maxwell's equation as a superposition of monochromatic waves. In this case, ϵ is taken to be a function of the frequency, ω:

$$\mathbf{D}(\omega) = \epsilon(\omega)\mathbf{E}(\omega). \tag{1.14}$$

The frequency-dependent dielectric function provides a complete description, in the classical picture, of the optical response of materials. It is the unusual nature of

this dielectric function for noble metals that is responsible for their unique plasmonic response. Developing a classical model for metal-nanoparticle plasmonics thus requires a model for the dielectric function of metals.

1.1.2 Bulk Plasmons and the Dielectric Function of Metals

The simplest model for the dielectric response of a metal is known as the Drude or free-electron model. In the Drude model, the conduction electrons are modeled as a gas of free, noninteracting electrons, which relax through collisions with the lattice or other scatterers. Experiments have shown that such a model works well as a first description of many simple metals, particularly at lower frequencies. One might wonder why the response of the sea of conduction electrons, moving inside a crystal and coupled via the electron–electron Coulomb interaction, can be modeled as a noninteracting gas. The accuracy of this simple, classical model actually arises from the quantum-mechanical nature of the electrons in the metal. The lattice defines a periodic potential for the electrons, with potential minima located at each of the positive ion cores. To first order, these ions can be considered as fixed in place. This means that the wavefunction of an electron moving in this potential landscape can be written as a product of a plane-wave envelope function and a periodic function, known as a Bloch function, that has the same periodicity as the lattice. The Schrödinger equation that governs the electron motion separates into a part that describes the envelope function and a stationary part that describes the Bloch functions. The electron motion is thus determined by the behavior of the plane-wave envelope functions. For simple metals, the Schrödinger equation describing these envelope waves is nearly identical to the equation describing free electrons. Because the resulting envelope wave functions are extended throughout the lattice, any particular conduction electron interacts primarily with the average potential produced by all the other conduction electrons in the system. This average, or mean-field interaction dominates over any interaction between pairs of electrons, so that each conduction electron can be treated as a noninteracting electron moving in a potential defined by this average field. One again ends up being able to treat the system as if it were made up of noninteracting, free electrons. In the simplest case, these quasi-free electrons differ from truly free electrons only in that they have an effective mass that is different from the mass of a free electron. In noble metals such as silver and gold, the effective electron mass is nearly identical to the bare electron mass.

In the end, this all means that, for a bulk crystal of a simple metal, one can leave quantum mechanics behind and describe electron motion in the lattice using a simple classical model of a free-electron gas:

$$m\frac{d^2x}{dt^2} = -\frac{m}{\tau}\frac{dx}{dt} - qE_{\text{tot}}(t), \tag{1.15}$$

where m is the electron effective mass, q is the charge of the electron, τ is a decay time to account macroscopically for electron scattering, and $E_{\text{tot}}(t)$ is the total electric field acting on the electron, including any external field and the internal field

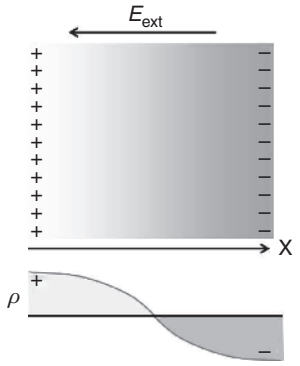

FIGURE 1.1 Schematic of a bulk plasmon responding to an external field. The shaded area in the top panel is a snapshot of the spatial distribution of induced charge polarization. The lower panel shows the one-dimensional charge distribution.

generated by the electron motion. Here, we describe one-dimensional motion defined by the direction of the driving field, where x is the displacement of the electron relative to the fixed background of atomic cores (see Figure 1.1). For an oscillatory applied field with frequency ω, the spatial displacement and any induced field will oscillate at the same frequency ω, so that $E_{\text{tot}}(t) = \text{Re}[E_{\text{tot}}(\omega)\exp(-\imath\omega t)]$ and $x(t) = \text{Re}[x(\omega)\exp(-\imath\omega t)]$. This gives

$$x(\omega) = \frac{q\,E_{\text{tot}}(\omega)}{m(\omega^2 + \imath\omega/\tau)}. \tag{1.16}$$

The induced polarization P arising when a two-dimensional sheet of conduction electrons is displaced by a distance x is

$$P(\omega) = -qx(\omega)n, \tag{1.17}$$

where n is the conduction electron density.

The dielectric function ϵ connects the displacement field and the polarization:

$$D(\omega) = \epsilon(\omega)E_{\text{tot}}(\omega) \equiv \epsilon_0(\omega)E_{\text{tot}}(\omega) + 4\pi\,P(\omega), \tag{1.18}$$

where $\epsilon_0(\omega)$ includes any dielectric response other than the polarization P from the conduction electrons. We thus get the following Drude form for the dielectric function of a free-electron metal:

$$\epsilon(\omega) = \epsilon_0(\omega) - \frac{\epsilon_0(\omega)\omega_{\text{p}}^2}{\omega^2 + \imath\omega/\tau}\,, \tag{1.19}$$

where the bulk plasmon frequency is

$$\omega_p = \sqrt{\frac{4\pi q^2 n}{\epsilon_0 m}}\,. \tag{1.20}$$

The total field acting on a conduction electron is any external driving field plus the induced field due to the displaced charge: $E_{\text{tot}}(\omega) = E_{\text{ext}}(\omega) + (4\pi nqx(\omega))/\epsilon_0$. Equation 1.15 can therefore be written as:

$$x(\omega)\left(\omega^2 + \frac{i\omega}{\tau} - \frac{4\pi nq^2 x}{\epsilon_0 m}\right) = \frac{q}{m}E_{\text{ext}}(\omega). \tag{1.21}$$

In the limit of zero damping, $\tau \to \infty$, the displacement at the bulk plasmon frequency, $x(\omega = \omega_{\text{p}})$, remains finite for an arbitrarily small driving field, corresponding to excitations of the conduction-electron gas. These excitations, known as bulk plasmons, are longitudinal in character, and arise in the limit of long wavelength and vanishing k (see Eq. 1.8). They propagate as charge-density waves, with peaks and valleys in the conduction-electron charge density developing along the propagation direction, analogous to peaks and valleys in matter density for a pressure or sound wave. Because bulk plasmons are longitudinal waves, they cannot couple directly to light, which is a transverse electromagnetic wave.

The limit of zero damping implies that the imaginary part of the dielectric function, $\epsilon_{\text{I}}(\omega)$, is zero. However, the dielectric function must satisfy the Kramers–Kronig relations, which provide a connection between $\epsilon_{\text{I}}(\omega)$ and the real part of the dielectric function, $\epsilon_{\text{R}}(\omega)$, and which imply that $\epsilon_{\text{I}}(\omega) \neq 0$. Finite damping means that the bulk plasmons have a finite lifetime. As explained in Section 1.2, below, it also means that plasmon resonances in metal nanoparticles are broadened.

Figure 1.2 compares empirical data for $\epsilon(\omega)$ for Au [6] with a fit to the Drude form (Eq. 1.19). At low frequencies (long wavelengths), the Drude model provides a good description of the dielectric response. In this regime, $\epsilon < 0$, the response is metallic, and the dominant contribution comes from the conduction electrons. As $\omega \to 0$, metallic screening of the external field that determines D becomes more and more perfect, and the total field becomes smaller and smaller. For a wide frequency range above ω_{p}, corresponding to photon energies of approximately 1–2 eV, ϵ_{I} is small, and plasmon modes in metal nanoparticles will be well defined. At higher frequencies, atomic-like transitions occur between d-band states and conduction-band states in gold. These transitions contribute to ϵ, so that the Drude model does not quantitatively or qualitatively reproduce the real dielectric function. There is a significant increase in ϵ_{I}, corresponding to significant damping of plasmon resonances. This discrepancy occurs even in the region where ϵ_{R} is near zero. In this region, plasmon resonances can occur, but the Drude model is not sufficient to quantitatively model these resonances.

One can extend the Drude model to include multiple poles described by different resonance frequencies and decay constants. This extended model is known as the

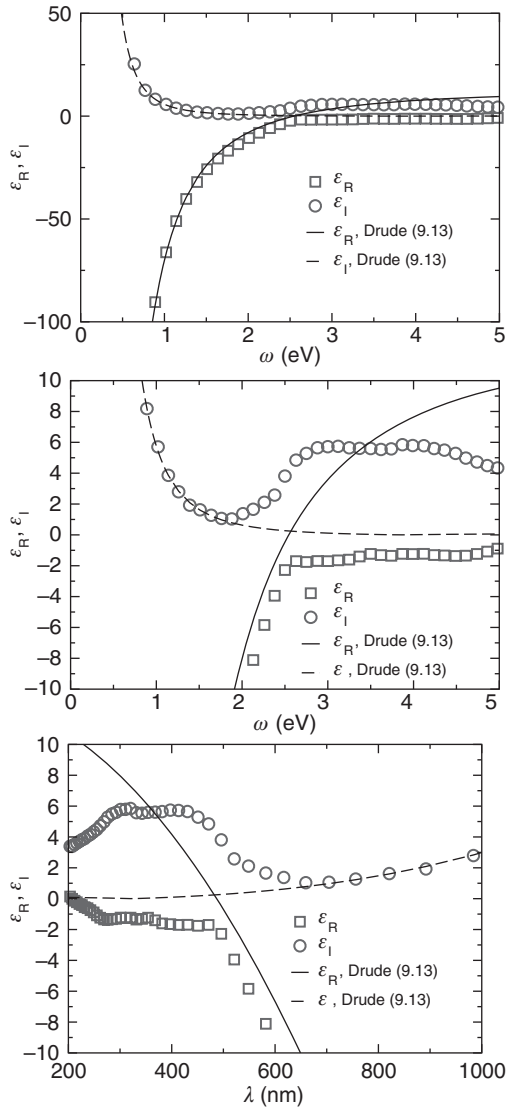

FIGURE 1.2 Top panel: Frequency dependence of the real and imaginary parts of the dielectric function of gold, ϵ_R and ϵ_I. The points indicate empirical values, and the lines show a fit to a Drude model. Middle panel: Expanded view of the region for ϵ_R near zero. Bottom panel: Wavelength dependence for the same region.

Lorentz–Drude model because Lorentzian lineshapes are used to model the contributions of interband transitions. The Lorentz–Drude model provides one approach to obtain more complicated analytical models that can better represent real metals. Such analytical models can be useful in numerical calculations, particularly those using finite-difference time-domain methods (see Section 1.3.1). However, in many

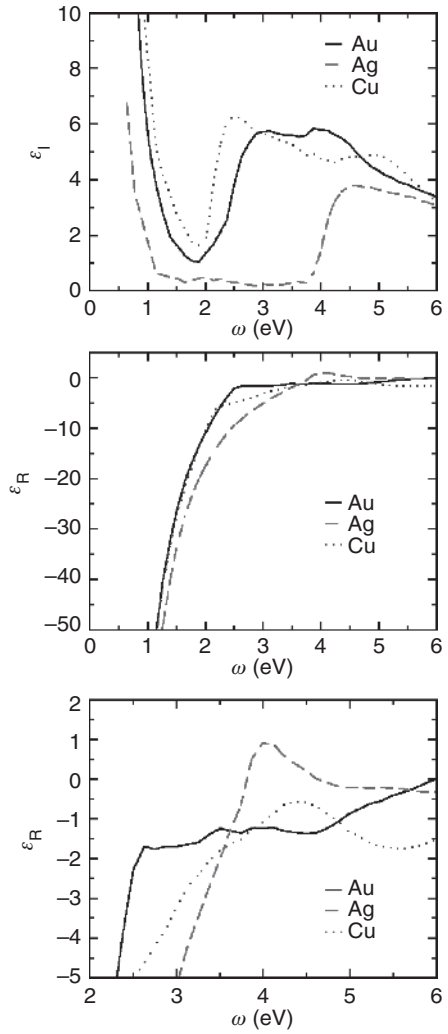

FIGURE 1.3 Comparison of tabulated empirical dielectric functions for Au, Ag, and Cu [6]. Top panel: Imaginary part of the dielectric function, ϵ_I. Middle panel: Real part of the dielectric function, ϵ_R. Bottom panel: Expanded view of ϵ_R in the region critical for plasmonics. There is significant uncertainty in the actual data, especially at low frequencies for ϵ_I.

cases, it is just as easy to use tabulated, empirical data, interpolating between data points to get a full $\epsilon(\omega)$. For most of the examples that we will discuss in this book, we use empirical data [6] to fully account for the effects of ϵ.

There are significant differences among the dielectric functions of different metals. Figure 1.3 compares empirical ϵ for Au, Ag, and Cu [6]. The ϵ_R for the three metals appear to be similar, with the Drude contribution dominating at low frequencies

and interband contributions prominent at higher frequencies. However, the expanded view shows there are important differences when ϵ_R is near zero, the region important for plasmonics, due to the different frequencies at which interband transitions begin to occur. The differences in ϵ_R mean that plasmon resonances for a particular nanoparticle shape will occur at different frequencies for the different metals. Even more importantly, the interband transitions produce large changes in ϵ_I, corresponding to large differences in plasmon damping. Ag has a wide window of low ϵ_I, and supports plasmon resonances with the lowest losses of all materials throughout most of the visible and near-infrared spectral regions. Cu has a much smaller window of lower losses, and is therefore not commonly used for plasmonic applications. Au is intermediate between the two other metals. However, Au is more chemically stable than Ag, and is therefore often used as the material of choice for plasmonic studies, despite having larger losses than Ag.

1.1.3 Surface-Plasmon Polaritons at Interfaces

When a bulk metal is terminated by a surface, new plasmons arise that are strongly localized to the surface. These "surface plasmons" propagate parallel to the surface but decay exponentially into the metal and into space away from the interface.

To characterize these surface plasmons, we consider an interface between two media, labeled 1 and 2. Defining the coordinate system such that the interface is located at $z = 0$ and the field propagates along the x direction (see Figure 1.4), the electric field in each region i has the form:

$$\mathbf{E}_i = (E_{ix}\hat{x} + E_{iz}\hat{z}) \exp\left[\imath(k_{ix}x + k_{iz}z - \omega t)\right]. \tag{1.22}$$

The phase of the field must be continuous across the interface, $k_{1x} = k_{2x} \equiv k_x$, and k_x is real. The wave is propagating along z in region i if k_{iz} is real, and is evanescent if k_{iz} is imaginary. Applying the boundary condition that the normal component of $\mathbf{D}$ is continuous across the interface, $\epsilon_1 E_{1z} = \epsilon_2 E_{2z}$, the condition that the waves be transverse, $k_{ix}E_{ix} + k_{iz}E_{iz} = 0$, and the dispersion relation in each region (Eq. 1.8), we obtain the dispersion relation for the interface modes:

$$k_x^2 = \frac{\epsilon_1 \epsilon_2 \omega^2}{(\epsilon_1 + \epsilon_2)c^2}. \tag{1.23}$$

For an interface between air ($\epsilon_1 = 1$) and a metal described by the Drude model with no damping ($\epsilon_2 = 1 - \omega_p^2/\omega^2$), the dispersion relation becomes

$$k_x^2 = \left(\frac{\omega^2 - \omega_p^2}{\omega^2 - \omega_s^2}\right)\left(\frac{\omega^2}{2c^2}\right), \tag{1.24}$$

with the surface-plasmon frequency $\omega_s \equiv \omega_p/\sqrt{2}$. Because $\mathbf{B}$ must be perpendicular to $\mathbf{E}$ and $\mathbf{k}$, the magnetic field lies in the surface plane; that is, the mode is transverse

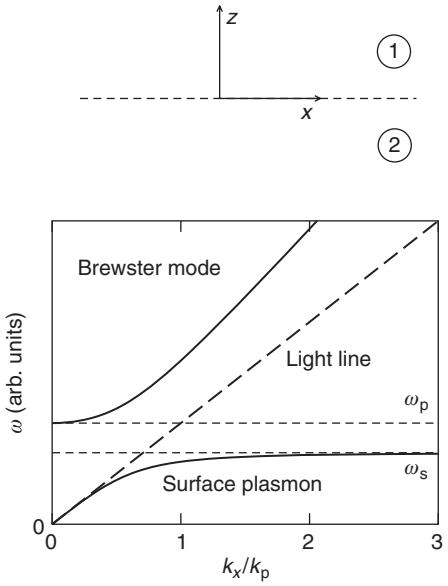

FIGURE 1.4 Top panel: Schematic of an interface between media 1 and 2. Bottom panel: Dispersion relation for the surface plasmon and the Brewster mode at a metal–air interface. The light line, bulk-plasmon frequency and surface-plasmon frequency are indicated. k_p is the plasmon wavevector, ω_p is the bulk plasmon frequency, and ω_s is the surface-plasmon frequency.

magnetic (TM). Here, we have assumed that **E** lies in the plane of incidence. A similar analysis shows that no transverse electric (TE) mode with **E** in the plane of the surface can exist.

From Equation 1.24, the condition that k_x be real for a propagating wave can be satisfied only for $\omega \geq \omega_p$ or $\omega \leq \omega_s$, as shown in Figure 1.4. It is easy to check that k_{1z} and k_{2z} are real if $\omega \geq \omega_p$, and both are imaginary if $\omega \leq \omega_s$. In the first case, the waves are propagating in both x and z. The mode is known as a Brewster mode, because it corresponds to an incident wave that can be transmitted from air into the metal without any reflection. From Equation 1.24, the Brewster mode arises when both ϵ_{R1} and ϵ_{R2} are positive, so that both regions act as dielectric materials. In the second case, for $\omega \leq \omega_s$, the modes are surface plasmons. The fields are localized near the surface, exponentially decaying away from the interface in both directions. For these modes to exist, one region must be metallic, with $\epsilon_R < 0$. As k_x increases, $k_z^2 \to -\infty$, indicating that fields become fully confined to the surface. In this limit, the charge density excited by the field is also fully localized to the surface. The fields and the charge-density oscillation are inextricably coupled; that is, the modes can be described as hybridization of the material charge density waves with electromagnetic waves propagating along the x direction. The propagating wave is therefore often referred to as a "surface-plasmon polariton," in order to emphasize the hybrid nature of the excitation. As can be seen from Figure 1.4, these mixed modes arise when the charge-density mode, which has flat dispersion, mixes at the surface with the

light field, which has linear dispersion. For $k_x = 0$, a longitudinal material mode exists, corresponding to the bulk-plasmon mode. The light mode evolves into the surface-plasmon mode and the bulk-plasmon mode evolves into the light mode as k_x increases.

The in-plane wavevector, k_x, of the surface plasmon is greater than the photon wave vector for all frequencies, as can be seen in Figure 1.4. Because the two in-plane wavevectors never match, light cannot couple directly to the surface plasmons. The wavevector mismatch can be overcome using a grating or other local modification of the surface, which provides the missing momentum, or by coupling through a high-refractive-index prism.

1.1.4 Guided Plasmon Modes in Wires

Several new effects arise when moving from a two-dimensional surface to a one-dimensional wire. First, charge oscillation around the wire must be periodic. This condition provides a quantization for the variation of the field in the azimuthal direction around the wire. Second, evanescent decay into the metal away from surface is no longer necessary to ensure a localized mode. Rather, localization in the metal can be provided by the finite cross-section of the wire, if the wire diameter is comparable to or smaller than the skin depth in the metal. In this case, the guided wire mode will differ strongly from the plasmon on a planar surface.

These effects are illustrated by the Sommerfeld modes of a cylindrical metal wire [5, 7, 8, 9]. Thinking of the wire as a rolled up two-dimensional sheet with periodic boundary conditions where the sheet edges connect, one expects the plasmon propagating along the nanowire to be a TM mode with a azimuthal **B** field, a radial electric field $\mathbf{E}_r$, and an electric field $\mathbf{E}_z$ along the wire axis z. The lowest-order, or fundamental mode will have a symmetric field with no azimuthal variation. For this mode, the radial electric field and the magnetic field satisfy the radial Bessel equation of order 1, whereas the longitudinal electric field satisfies the radial Bessel equation of order 0. The form of the electric field is thus

$$\mathbf{E} = \left(\mathbf{E}_r^{\text{in}} J_1(k_{\text{in}} r) + \mathbf{E}_z^{\text{in}} J_0(k_{\text{in}} r)\right) \exp\left(\imath(kz - \omega t)\right) , \qquad r \leq a \quad (1.25)$$

$$\mathbf{E} = \left(\mathbf{E}_r^{\text{out}} H_1(k_{\text{out}} r) + \mathbf{E}_z^{\text{out}} H_0(k_{\text{out}} r)\right) \exp\left(\imath(kz - \omega t)\right) , \qquad r \geq a \quad (1.26)$$

where a is the wire radius, k_{out} and k_{in} are the radial wavevectors outside and inside the metal, respectively, and k is the propagation constant along the wire. J is the Bessel function of the first kind and H is the Hankel function; these particular Bessel-function solutions ensure a finite field everywhere inside the wire and an evanescently decaying field away from the wire. k_{in} and k_{out} are determined from dispersion relations in each region:

$$k^2 + k_{\text{out}}^2 = \epsilon_{\text{out}} \frac{\omega^2}{c^2}, \quad (1.27)$$

and

$$k^2 + k_{\text{in}}^2 = \epsilon_{\text{in}} \frac{\omega^2}{c^2}. \tag{1.28}$$

A straightforward application of the boundary conditions leads to the following dispersion relation for k:

$$\frac{\epsilon_{\text{out}}}{k_{\text{out}}} \frac{H_1(k_{\text{out}}a)}{H_0(k_{\text{out}}a)} = \frac{\epsilon_{\text{in}}}{k_{\text{in}}} \frac{J_1(k_{\text{in}}a)}{J_0(k_{\text{in}}a)}. \tag{1.29}$$

Higher order azimuthal modes also exist. However, they are more strongly confined inside the wire, and are therefore more strongly damped by losses within the metal. As the wire diameter decreases, these modes become increasingly lossy, and eventually are effectively unbound to the wire. The fundamental mode, by contrast, has no cutoff, and remains bound to the metal nanowire for arbitrarily small diameters. For sufficiently small wire diameters, then, plasmon propagation is entirely dominated by the lowest-order mode.

The dispersion curve for this lowest-order mode is compared, in Figure 1.5, to the dispersion curve for a plasmon on a planar surface [10]. Inspection of the dispersion relation shows that the results for different wire radii scale with ka. As expected, at high frequencies (corresponding to small ka), the lowest-order wire mode and the surface plasmon mode follow the same dispersion. At low frequencies, the two dispersions differ significantly, due to different penetrations of the fields into the metal. Because of the surface curvature of the wire, fields penetrating into the wire can overlap and interfere constructively. This means that there is a higher optical energy density in the wire, and thus stronger dispersion of the propagating waves. These differences at low frequencies are further magnified because the skin depth increases as ω decreases [5].

1.2 DISCRETE PLASMON RESONANCES IN PARTICLES

The presence of a metal surface leads to propagating plasmon modes that are strongly localized at the surface. When the surface is rolled up into a wire, plasmons propagate along the wire in the axial direction. In the transverse direction, the field is quantized into discrete modes. For a metal nanoparticle, the charge oscillation and field distribution along the surface must be quantized in all three directions. As a consequence, the particle supports discrete plasmon modes. In other words, instead of propagating waves described by a wavevector, k, plasmons in nanoparticles form standing waves defined by the geometry of the particle.

The lowest-order mode of a spherical particle driven by an external field is illustrated in Figure 1.6. This mode is dipole-like, with negative charge accumulating on one side of the particle and positive charge accumulating on the opposite side. Field

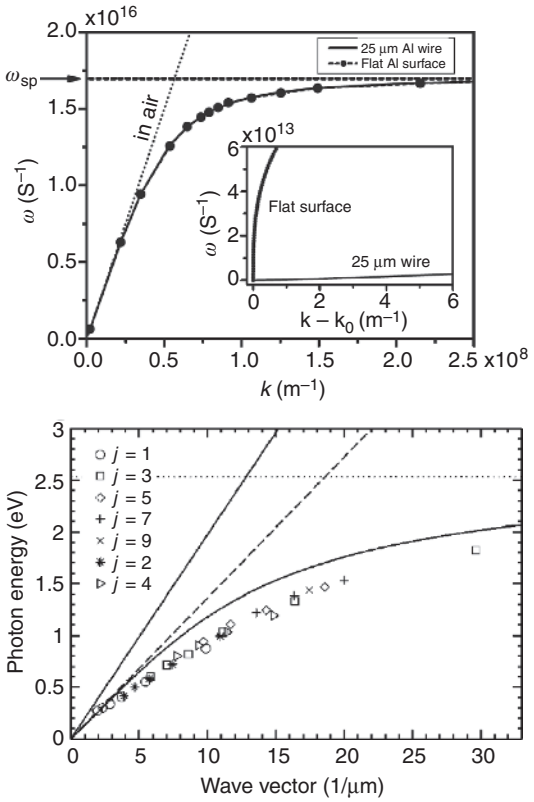

FIGURE 1.5 Top panel: Calculated dispersion relation for the surface plasmon on a planar Al surface and for the lowest order mode of a circular Al wire with a diameter of 25 μm. ω_{sp} is the surface-plasmon frequency. The linear dispersion of the light line is indicated. The inset shows the dispersion relations at low frequency. In the inset, ω is plotted versus $(k - k_o)$ where k_o is the propagation wavevector for light. In this case, the light line is vertical at $(k - k_o) = 0$. Reprinted with permission from Reference [10]. Copyright (2006) American Physical Society. Bottom panel: Dispersion relation for the surface plasmon on a planar gold surface compared with the measured plasmon dispersion of a rectangular gold nanowire with width 91 nm and height 17 nm. The solid line is the light line in vacuum, and the dashed line is the light line in the quartz substrate that supports the Au nanowire. The solid curve is the dispersion for a thin gold layer on the substrate. The dotted line is ω_{sp}. The symbols are measured values for plasmons in gold nanowires with different lengths. The index j indicates the number of half-waves on the wire. Reprinted with permission from Reference [11]. Copyright (2003) American Physical Society.

lines converge at the regions where the charges accumulate, corresponding to strong local enhancement of the electric fields.

Particles with different shapes will support different modes. For example, a nanorod that is extended in one direction will support longitudinal modes when an external field drives the charge along the long axis of the rod, and will support transverse modes when the charge is driven along the short dimension, as illustrated in Figure 1.6. The lowest-order longitudinal mode is similar to the lowest-order

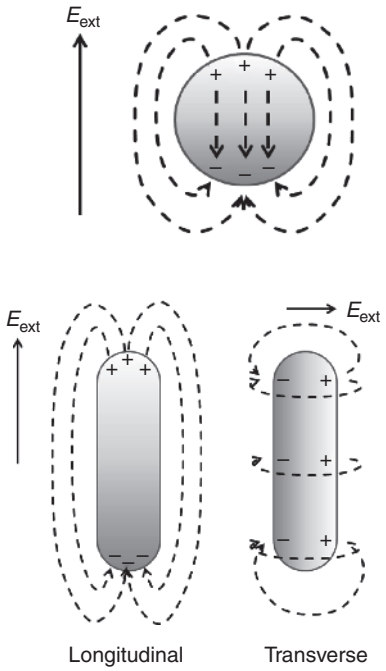

FIGURE 1.6 Top panel: Schematic for the dipolar mode of a spherical particle driven by an external field E_{ext}. The field lines produced by the plasmon resonance are indicated. Bottom panel: Schematic for the lowest-order longitudinal and transverse modes of a nanorod.

mode in the sphere, with strong concentration at the rod ends. The transverse mode results in very different field distributions, and occurs at a different frequency than the longitudinal mode.

Although the nanoparticle modes occur at discrete frequencies, they are strongly broadened by the significant damping in the metal. They are thus not truly discrete modes, but should rather be thought of as resonances of the structure. At frequencies where metal losses are relatively small, the resonances can be well defined; if metal losses are large, by contrast, the response of the metal nanoparticle becomes broad, and it can be difficult to determine a specific resonance frequency. We will often use the word "mode" to refer to plasmon resonances in metal nanoparticles, but it is important to keep in mind the differences between these rapidly decaying excitations and true eigenmodes.

Several viewpoints provide an intuitive picture for the origin of plasmon resonances in metal nanoparticles. From our discussion of surface plasmons at planar surfaces and on nanowires, one should expect that plasmons in metal nanoparticles are excitations localized at the particle surface, completely quantized because the particle surface is a planar surface rolled up in both dimensions. Multiple modes should be possible, defined by the quantization to ensure that multiple half waves of the excitation fit along the particle surface. This works well when the nanoparticle is

much larger than the skin depth, so that the mode is strongly localized to the metal surface, and when it is much larger than the plasmon wavelength, so that multiple modes are supported.

In the opposite limit, when the nanoparticle is much smaller than the plasmon wavelength and the skin depth, the entire particle is driven in phase by the same electric field, and localization is provided by the size of the particle rather than by internal damping. The particle can then be approximated as a dipole, and the response to external fields can be quantified by an effective dipole moment. Higher order modes are absent in this limit, so that the details of the particle geometry are important only for defining the effective dipole moment. This picture works well to describe fields far from small particles. Close to a particle, even if the particle is very small, the local geometry is critical for determining the local field. The validity of the viewpoint, in other words, depends not only on the size of the particle but also on the fields that are being considered.

Perhaps the most compelling and intuitive picture of plasmons in metal nanopartices, one which ties together the other two pictures, is that the resonances correspond to displacements of the conduction electron density toward one side of the particle by an applied driving field. This sets up a restoring force between the negatively charged electrons and the positively charged ion cores that are left behind. If the conduction electron density is incompressible, then charge can accumulate only at the surface, as indicated in Figure 1.6. Net positive and negative charges appear on opposite surfaces of the nanoparticle, and the strength of the restoring force depends on the distribution of these charges. The restoring force, in turn, defines the oscillation frequency. The plasmon resonance thus depends on the shape of the nanoparticle, which determines how the charge accumulates at different positions on the surface, and on the electron density, which determines the amount of charge that accumulates. The high electron densities in noble metals lead to plasmon resonance at visible and near-infrared frequencies. The surface charges are also responsible for the strong local fields at the surfaces of the particles that arise when the plasmon resonances are excited.

1.2.1 Metal Spheres in the Quasistatic Approximation

Small, spherical metal particles are the simplest structures that support discrete plasmon resonances. Under certain circumstances, the optical response of these particles can be described using straightforward analytical expressions. Although a number of approximations must be made in order to obtain a simple description of the nanoparticle response, the insight provided by the simple expressions serves as a basis for understanding more complex structures.

The key approximation we will make here is that the particle diameter, a, is much smaller than the wavelength, λ, of the external, driving field. This is known as the "quasistatic" approximation, because it allows retardation effects to be ignored. That is, the variation of the phase of the external field across the particle is negligible, so an incident plane wave can be approximated by a constant field. Maxwell's equations can then be solved in terms of an electric potential, Φ, where $\mathbf{E} = -\nabla\Phi$. For a driving field applied in the z direction, the applied potential is $\Phi = -Ez$, or, in polar

coordinates, $\Phi = -Er\cos(\theta)$. Potentials inside and outside of the metal particle can be written in terms of Legendre polynomials $P_\ell(\theta)$:

$$\Phi_{\text{in}}(r,\theta) = \sum_{\ell=1}^{\infty} A_\ell r^\ell P_\ell(\cos(\theta))\,, \tag{1.30}$$

for $r \leq a$, and

$$\Phi_{\text{out}}(r,\theta) = \sum_{\ell=1}^{\infty} B_\ell r^{-(\ell+1)} P_\ell(\cos(\theta)) - Er\cos(\theta)\,, \tag{1.31}$$

for $r \geq a$, where a is the radius of the particle.

Applying the boundary conditions that the potential and the normal component of $\mathbf{D}$ are continuous at $r = a$, we get

$$\ell = 0: \quad A_0 = B_0 = 0\,, \tag{1.32}$$

$$\ell = 1: \quad A_1 = \frac{-3\epsilon_{\text{out}}E}{\epsilon_{\text{in}} + 2\epsilon_{\text{out}}}, \quad B_1 = \frac{(\epsilon_{\text{in}} - \epsilon_{\text{out}})Ea^3}{\epsilon_{\text{in}} + 2\epsilon_{\text{out}}}\,, \tag{1.33}$$

$$\ell > 1: \quad -\frac{\epsilon_{\text{out}}}{\epsilon_{\text{in}}}\frac{\ell+1}{\ell} = 1, \quad A_\ell = \frac{B_\ell}{a^{2\ell+1}}\,. \tag{1.34}$$

In these expressions, ϵ_{in} is the dielectric function of the metal particle and ϵ_{out} is the dielectric function of the surrounding medium.

There is no constant ($\ell = 0$) term, as such a term would represent a net charge on the particle. For $\ell = 1$, there is a response at any frequency, provided there is a driving field to excite the particle. However, when $\text{Re}[\epsilon_{\text{in}} + 2\epsilon_{\text{out}}] = 0$, A_1 and B_1 take on large values. In the absence of damping (i.e., for $\text{Im}[\epsilon_{\text{in}}] = \text{Im}[\epsilon_{\text{out}}] = 0$), the coefficients become singular, indicating that a mode exists that is excited for arbitrarily small driving fields. For $\ell > 1$, the response is independent of E, indicating that higher order modes cannot be excited by a constant field.

The metal nanoparticle thus acts like a dipole with a resonance frequency of ω_1. In the quasistatic limit, the potential of a dipole with dipole moment μ pointed along z is $\Phi = \mu z/\epsilon_{\text{out}} r^3$ [5]. Comparing with the form of Φ_{out} for the metal nanoparticle, we obtain

$$\alpha = \frac{(\epsilon_{\text{in}} - \epsilon_{\text{out}})\epsilon_{\text{out}}a^3}{\epsilon_{\text{in}} + 2\epsilon_{\text{out}}}\,, \tag{1.35}$$

where $\alpha \equiv \mu/E$ is the polarizability of the particle. Inside the particle, the electric field is constant, but is reduced, compared with the external field, because of the

screening by conduction electrons in the metal. The field is reduced by the screening factor

$$\mathrm{SF} = \frac{3\epsilon_{\mathrm{out}}}{\epsilon_{\mathrm{in}} + 2\epsilon_{\mathrm{out}}}\,. \tag{1.36}$$

If the sphere is in air or vacuum, so that $\epsilon_{\mathrm{out}} = 1$, and the dielectric function of the metal is approximated by the Drude model without damping, then the screening factor and polarizability take on simple forms:

$$\mathrm{SF}_{\mathrm{Drude}} = \frac{\omega^2}{\omega^2 - \omega_1^2}, \tag{1.37}$$

and

$$\alpha_{\mathrm{Drude}} = \frac{-\omega_1^2 a^3}{\omega^2 - \omega_1^2}. \tag{1.38}$$

At $\omega = 0$, the Drude particle becomes a perfect conductor, and $\mathrm{SF}_{\mathrm{Drude}} = 0$, indicating that the internal field is perfectly screened. As $\omega \to \omega_1$, the response becomes resonant. For $0 < \omega < \omega_1$, the internal field is larger than but out of phase with the external field. For $\omega > \omega_1$, the internal field is enhanced and is in phase with the external field. For large ω, the internal response can no longer follow the applied field, and the field inside is the unscreened external field. The dipole polarization is also resonant at ω_1. It is in phase with the driving field below ω_1 and out of phase above the resonance, consistent with the phase of the internal field. For small ω, the polarizability, α, is equal to the static polarizability, a^3. For large ω, α vanishes and there is no induced dipole because the particle response cannot follow the driving field.

Although only a single, dipole resonance can be excited by an incident plane wave, higher order external fields with more complex phase fronts can excite higher order resonances, at frequencies that satisfy

$$(\ell + 1)\epsilon_{\mathrm{out}} = -\ell\epsilon_{\mathrm{in}}. \tag{1.39}$$

For a Drude metal without any damping, these resonances occur at

$$\omega_\ell = \omega_{\mathrm{p}}\sqrt{\ell/(\ell + (\ell + 1)\epsilon_{\mathrm{out}})}\,. \tag{1.40}$$

The ω_ℓ lie between the lower limit defined by ω_1 and the upper limit determined by the surface plasmon frequency, $\omega_{\mathrm{p}}/\sqrt{\epsilon_{\mathrm{out}} + 1}$. In the quasistatic limit, the ω_ℓ are independent of particle size. We will see later that the modes become size-dependent when the quasistatic approximation fails and fully retarded, time-dependent solutions to Maxwell's equations are required. We will see in Section 1.4.3 that this breakdown

of the quasistatic approximation can occur for quite small particle sizes, well before the diameter is comparable to the free-space optical wavelength.

In the quasistatic limit, the polarizability α can be used directly to calculate the optical absorption and scattering cross-sections of the particle. The absorption cross-section, σ_{abs}, is defined as the rate at which optical energy is absorbed by the particle, divided by the incident optical flux (energy flow per unit area); similarly, the scattering cross-section, σ_{scat}, is defined as the rate at which optical energy is scattered by the particle, divided by the incident flux. In terms of α, the cross sections are

$$\sigma_{\text{abs}} = \frac{4\pi k}{\epsilon_{\text{out}}} \text{Im}[\alpha] \,, \tag{1.41}$$

and

$$\sigma_{\text{scat}} = \frac{8\pi \omega^4}{3c^4} |\alpha|^2 \,, \tag{1.42}$$

where k is the wavevector in the medium. Using Equation 1.35 for small spheres,

$$\sigma_{\text{abs}} = 4\pi k a^3 \text{Im}\left[\frac{\epsilon_{\text{in}} - \epsilon_{\text{out}}}{\epsilon_{\text{in}} + 2\epsilon_{\text{out}}}\right] \tag{1.43}$$

and

$$\sigma_{\text{scat}} = \frac{8}{3}\pi k^4 a^6 \left|\frac{\epsilon_{\text{in}} - \epsilon_{\text{out}}}{\epsilon_{\text{in}} + 2\epsilon_{\text{out}}}\right|^2 . \tag{1.44}$$

Clearly, the cross-sections vanish if the medium and the nanoparticle are the same. When they are different, the absorption cross-section scales as a^3 and the scattering cross-section scales as a^6. Intuitively, the absorption scales as the volume, V, of the particle. The scattering scales as V^2 because scattering involves absorption and reemission of the light (although these processes occur instantaneously, and no energy is transferred from the light to the particle). Scattering in this limit, where the particle is much smaller than the wavelength of light, is often referred to as Rayleigh scattering.

Figure 1.7 shows calculated absorption and scattering cross-sections of spherical Au nanoparticles in the quasistatic limit. The dipole plasmon resonance is seen near a wavelength of 500 nm. At shorter wavelengths, the contribution from the interband transitions is dominant. This can be clearly seen in the middle panel, which compares to the predictions of the Drude model, where the interband contribution is absent. Using the Drude model, the same plasmonic peak is clearly present, but its magnitude is dramatically overestimated.

In Figure 1.7, calculated cross-sections are normalized by the geometric cross-section of the sphere, in order to indicate the relative magnitude of the cross-sections. For the particle sizes shown in the top panel, the absorption and scattering cross-sections are comparable to the geometrical cross-section. However, the normalized

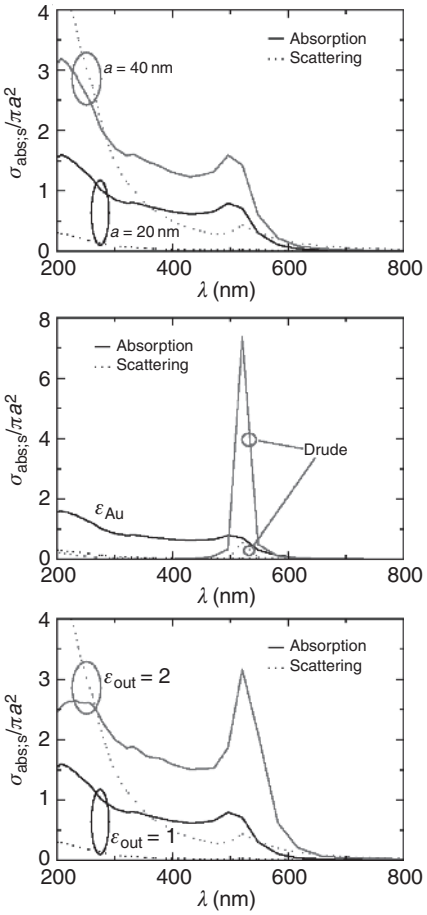

FIGURE 1.7 Absorption and scattering cross-sections, σ_{abs} and σ_s, for a gold nanosphere with radius a. The cross-sections are calculated in the quasistatic limit and are normalized by the geometrical cross-section of the sphere. The top panel shows the dependence on a for the dielectric constant of the surroundings, $\epsilon_{out} = 1$. The middle panel compares results of a calculation using empirical data for the dielectric function of gold [6] with calculations using a Drude model, for a sphere with $a = 20$ nm and $\epsilon_{out} = 1$. The bottom panel shows the dependence on ϵ_{out} for $a = 20$ nm.

absorption cross-section scales linearly with a and the normalized scattering cross-section scales with a^4, so they become much larger than the geometrical cross-section as a increases. The absorption cross-section is larger than the scattering cross-section for small a, but for $a > 40$ nm, the scattering cross-section becomes larger. This is especially true at short wavelengths, as the scattering cross-section also scales as $1/\lambda^4$. There is a small shift between the plasmon peaks for absorption and scattering.

The bottom panel shows the dependence of the cross sections on ϵ_{out}. Two effects can be seen. First, $k = \sqrt{\epsilon_{out}}\omega/c$, so the absorption and scattering cross-sections scale with $\sqrt{\epsilon_{out}}$ and ϵ_{out}^2, respectively. In addition, the resonance shifts to lower frequency,

from $\omega_p/\sqrt{3}$ to $\omega_p/\sqrt{3\epsilon_{out}}$, because the medium screens the Coulomb restoring force that determines the plasmonic response. The dependence of the plasmon resonance frequency on the dielectric constant—or, equivalently, the refractive index—of the medium is a universal property of plasmon resonances in metal nanoparticles. It can be used as a means of detecting local changes in refractive index, as discussed in Section 7.1.

1.2.2 Spheroids in the Quasistatic Approximation

Having seen that spherical metal nanoparticles support size-independent plasmon resonances in the quasistatic limit, we now consider how the modes change when the particle deviates from spherical symmetry while remaining in the quasistatic limit. There are very few geometries that can be studied analytically, but one nanoparticle geometry that does allow for analytical solutions is an ellipsoid [12]. Such particles have a surface defined by

$$\frac{x^2}{a^2} + \frac{y^2}{b^2} + \frac{z^2}{c^2} = 1, \tag{1.45}$$

where a, b, and c are the semi-axes of the particle. For $a = b = c$, an ellipsoid is a sphere, so ellipsoids provides an straightforward way to study shape effects as the particle geometry evolves away from a sphere.

The solution for an ellipsoidal particle proceeds via two steps. First, the problem is formulated in ellipsoidal coordinates. Once the coordinate transformation is made, the field response to a plane wave is determined in the quasistatic limit, as was done for spherical particles. Full derivations are available elsewhere [12]; here, we simply provide the solutions in order to understand the effect of shape on particle response.

Inside the particle, the field is constant, as for a sphere, but with a different screening factor:

$$\mathrm{SF} = \frac{\epsilon_{out}}{\epsilon_{out} + L(\epsilon_{in} - \epsilon_{out})}, \tag{1.46}$$

where the geometrical factor L is given, for an applied field along z, by

$$L = \frac{abc}{2} \int_0^\infty \frac{ds}{(c^2 + s)g(s)}, \tag{1.47}$$

where

$$g(s) = \sqrt{(a^2 + s)(b^2 + s)(c^2 + s)}. \tag{1.48}$$

Equivalent expressions are obtained for applied fields along x or y. The far-field response of the particle is again that of a dipole, but now with a polarizability

$$\alpha = \frac{abc(\epsilon_{\text{in}} - \epsilon_{\text{out}})\epsilon_{\text{out}}}{3(\epsilon_{\text{out}} + L(\epsilon_{\text{in}} - \epsilon_{\text{out}}))}. \tag{1.49}$$

L determines the effect of shape. It depends only on the relative dimensions of the particle and not on the overall size of the particle. In other words, the quasistatic approximation again gives a response that is independent of particle size, but that now depends on the nanoparticle geometry.

The effect of shape can be appreciated by again considering a particle in air whose dielectric function is described by a Drude model without damping. In that case,

$$\text{SF}_{\text{Drude}} = \frac{\omega^2}{\omega^2 - L\omega_{\text{p}}^2}, \tag{1.50}$$

and

$$\alpha_{\text{Drude}} = \frac{-\omega_{\text{l}}^2 abc}{\omega^2 - L\omega_{\text{p}}^2}. \tag{1.51}$$

SF_{Drude} and α_{Drude} have a resonance at $\omega_{\text{p}}\sqrt{L}$. For a sphere, $L = 1/3$ and $\omega_{\text{p}}\sqrt{L} = \omega_{\text{p}}/\sqrt{3} = \omega_{\text{l}}$. Changing the ratios of a, b, and c changes the value of L, and thus shifts the resonance frequency.

L can be evaluated easily for special classes of ellipsoids, including prolate spheroids, where $a = b$, and oblate spheroids, where $a = c$. Prolate spheroids become elongated, rod-like nanoparticles as c increases, and oblate spheroids become flattened disks as c decreases. In both cases, $L_z \to 0$ as the particle shape evolves away from a sphere (see Figure 1.8). As a consequence, the resonance frequency shifts to lower frequencies. For prolate spheroids, this low-frequency resonance is the longitudinal plasmon mode. In this case, the reduced resonance frequency can be understood as a consequence of a reduced restoring force between the charges that accumulate on opposite ends of the rods. By contrast, L_x and L_y increase as the rod becomes more elongated, corresponding to an increase in the frequency of the transverse plasmon mode.

For oblate spheroids, one might expect that evolving from a sphere to a disk would shift the resonance frequency toward the frequency $\omega_{\text{s}} = \omega_{\text{p}}/\sqrt{2}$ for a single surface. However, the disk is actually two flat surfaces close together, and plasmon modes on the top and bottom surfaces couple to one another when the disk is thin. The coupled plasmons form symmetric and antisymmetric modes. The symmetric mode, with charge on the top and bottom surfaces moving together in phase, shifts to lower frequencies, and the antisymmetric mode shifts to higher frequencies. Only the red-shifted symmetric mode is excited by an incident plane wave. This is a first example of plasmon coupling effects, which will be discussed in detail in Chapter 4.

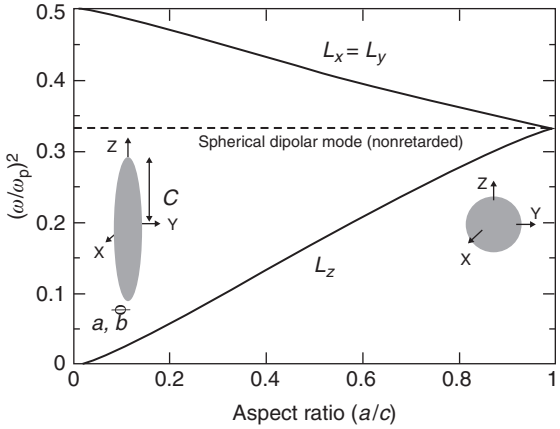

FIGURE 1.8 Shape dependence of the longitudinal and transverse modes of a prolate spheroidal metal nanoparticle in the quasistatic limit. ω_p is the bulk plasmon frequency.

For both classes of spheroids, the common factor is that moving from a sphere toward lower-symmetry shapes produces a resonance that is shifted towards lower frequencies. This is a general property of plasmonic metal nanoparticles: small, sharp features generally produce red-shifted resonances. Although it is not immediately obvious here, the "pointy" features also lead to strong enhancement of the local electric field.

Equations 1.41 and 1.42 for the absorption and scattering cross-sections of small spheres can be generalized to cover spheroids. The average absorption and scattering cross-sections, in the quasistatic limit, for a collection of randomly oriented spheroids are [12]

$$\sigma_{\text{abs}}^{\text{avg}} = \frac{4\pi k}{\epsilon_{\text{out}}} \text{Im}\left[\frac{1}{3}\alpha_1 + \frac{1}{3}\alpha_2 + \frac{1}{3}\alpha_3\right], \tag{1.52}$$

and

$$\sigma_{\text{scat}}^{\text{avg}} = \frac{8\pi\omega^4}{3c^4}\left(\frac{1}{3}|\alpha_1|^2 + \frac{1}{3}|\alpha_2|^2 + \frac{1}{3}|\alpha_3|^2\right), \tag{1.53}$$

where the α_i are the polarizabilities along the three principle axes.

1.2.3 Multipolar Response and Mie Theory

So far, we have considered only particles in the quasistatic limit. This limit holds when the particle is much smaller than the optical wavelength. For larger particles, the optical response becomes much more complicated; this can start to occur even for particles as small as 10% of the wavelength. An incident plane wave can excite higher order modes in these particles, not just the dipolar mode. In order to understand how

these higher order modes are excited, we must considered a fully retarded theory for the particle response. Here, we will briefly describe the aspects of such a theory for spherical particles.

The development of a theory of multipole fields starts from a solution of Maxwell's equations in spherical coordinates (r,θ,ϕ) for a homogeneous, source-free region [5]. Two classes of solutions are possible. One class is known as TM, because the magnetic field is transverse to the radial vector; they are also sometimes referred to as electric modes because they are excited by incident electric fields. These solutions take the form

$$\mathbf{B}_{\ell m} = \Psi(kr)\mathbf{X}_{\ell m}(\theta,\phi)\,, \tag{1.54}$$

$$\mathbf{E}_{\ell m} = \frac{\imath}{k}\nabla\times\mathbf{B}_{\ell m}\,, \tag{1.55}$$

with

$$\mathbf{X}_{\ell m}(\theta,\phi) = \frac{1}{\sqrt{\ell(\ell+1)}}\mathbf{L}Y_{\ell m}(\theta,\phi)\,, \tag{1.56}$$

where $k=\sqrt{\epsilon}\omega/c$, $\mathbf{L}$ is the angular momentum operator, $Y_{\ell m}$ is a spherical-harmonic function, and $\Psi(kr)=a_\ell^1 h_\ell^1(kr)+a_\ell^2 h_\ell^2(kr)$ is a linear combination of the two spherical Hankel functions of order ℓ. ($\Psi(kr)$ can also be written as a linear combination of any other pair of spherical Bessel functions of order ℓ that have the appropriate behavior at large and small r.)

A second class of solutions are the TE modes, where the electric field is transverse to the radial vector; these are also sometimes referred to as magnetic modes. The TE modes are dual to the TM modes:

$$\mathbf{E}_{\ell m} = \Psi(kr)\mathbf{X}_{\ell m}(\theta,\phi) \tag{1.57}$$

$$\mathbf{B}_{\ell m} = \frac{-\imath}{k}\nabla\times\mathbf{E}_{\ell m}. \tag{1.58}$$

Any field can be expressed in spherical coordinates as a sum over ℓ and m of the TM and TE modes.

A circularly polarized plane wave field can be written as [5]

$$\begin{aligned}\mathbf{E}_\pm(\mathbf{r}) &= (\hat{x}\pm\imath\hat{y})\exp(\imath kz)\\ &= \sum_{\ell=1}^{\infty}\imath^\ell\sqrt{4\pi(2\ell+1)}\left[j_\ell(kr)\mathbf{X}_{\ell,\pm1}\pm\frac{1}{k}\nabla\times j_\ell(kr)\mathbf{X}_{\ell,\pm1}\right]\end{aligned} \tag{1.59}$$

where j_ℓ is the spherical Bessel function regular at the origin. Only terms for $m=\pm1$ appear, corresponding to the two circular polarizations. In the quasistatic limit, $kr\to0$, only the $\ell=1$ terms remain finite and a plane wave couples only to dipolar fields. In the fully retarded limit, the full expansion must be used.

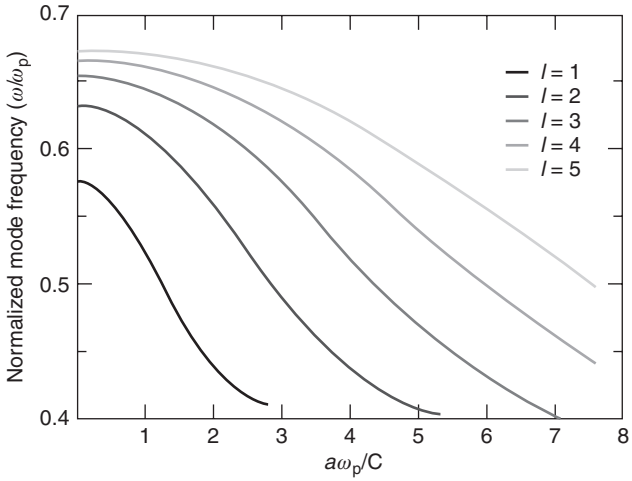

FIGURE 1.9 Size dependence of the first five Mie modes of a sphere with radius a. ω_p is the bulk plasmon frequency and l is the order of the mode. From Reference [13]. Copyright 2008 Wiley-VCH Verlag GmbH & Co. KGaA, Weinheim.

The full solution for the local and far fields scattered by a spherical metal particle is known as Mie theory, and was developed a hundred years ago [14]. Just as with any of the cases we have already considered, one starts by writing the fields inside and outside the metal sphere in terms of the TM and TE fields (Eqs. 1.54–1.58). Boundary conditions at the sphere surface connect the fields inside and outside and establish linear equations for the expansion coefficients. These equations can be solved in terms of spherical Bessel and Hankel functions that define the radial variation of the field at the particle surface. Such solutions, while elegant, are straightforward to understand only in special limits when the Bessel and Hankel functions take simple forms. Otherwise, numerical evaluation of the functions is necessary. Figure 1.9 shows the results of such numerical evaluation for first five Mie modes.

Because evaluation of Mie scattering is a numerical exercise, we will not discuss it further, but will instead move on to a discussion of other methods to evaluate Maxwell's equations numerically. We will then discuss the results of these numerical simulations for representative particle geometries in order to see how the near-field and far-field response of the particles depend on their size and shape.

1.3 OVERVIEW OF NUMERICAL METHODS

We have provided analytical solutions for the plasmon modes of a few simple geometries, including planar interfaces, cylinders, spheres, and spheroids. Analytical and semi analytical solutions have been found for a number of other geometries, including cubes [15], edges [16], and hemispheres [17]. However, these theories often rely on

simple models for the dielectric response, such as the Drude model. Obtaining quantitative theoretical results based on accurate, empirical dielectric functions generally requires the use of computational approaches. Moreover, numerical approaches are unavoidable when attempting to understand the optical response of more complicated structures. A number of numerical methods have therefore been developed to handle arbitrary geometries. Among the most commonly used are the finite-difference time-domain (FDTD) method [18], the discrete dipole approximation (DDA) [19, 20], Greens-function approaches similar in spirit to the DDA [21], the multiple multipole (MMP) method [22], multiple scattering techniques, transfer-matrix approaches [23], plane wave expansions [24], and boundary element methods (BEM) [25].

All of these computational approaches have advantages and disadvantages. Plane wave expansions and transfer-matrix approaches work well if a limited number of expansion functions can accurately represent the fields of the structure. This can be the case for extended wavelength-scale objects and for arrays of NPs. These approaches are more difficult to apply for small, nanometer-scale, subwavelength individual NPs with arbitrary geometry, for strongly coupled, closely spaced NPs, and for structures for multiple length scales. Real-space techniques are therefore most commonly employed to directly obtain the near-field and far-field response of complicated metal nanostructures. We review some of these real-space approaches here.

1.3.1 FDTD Methods

The FDTD method is an intuitively straightforward approach because it involves solving Maxwell's equations directly. The fields are discretized in time and in space, on a grid that encompasses the nanoparticles to be studied and a surrounding region in which the field is to be determined. Fields are found explicitly by propagating discrete versions of Maxwell's equations forward in time.

To get a feeling for how this is usually done, consider one of Maxwell's curl equations:

$$\nabla \times \mathbf{E} = -\frac{1}{c}\frac{\partial \mathbf{B}}{\partial t}. \tag{1.60}$$

Using a central difference expression for the time derivative, this can be written as

$$\mathbf{B}(\mathbf{x}, t + \delta t) = \mathbf{B}(\mathbf{x}, t - \delta t) - 2(\delta t)c\nabla \times \mathbf{E}(\mathbf{x}, t). \tag{1.61}$$

$\mathbf{B}$ at time $(t + \delta t)$ can be found from this equation if $\mathbf{B}$ at time $(t - \delta t)$ and $\mathbf{E}$ at time t are known. In a similar manner, the other Maxwell curl equation can be used to propagate $\mathbf{E}$ forward in time. As a result, $\mathbf{E}$ and $\mathbf{B}$ are defined on two different time grids, each with a time step of $2\delta t$, but shifted by δt. In a similar manner, the curl operator can be expanded as a sum of central differences. As a consequence, $\mathbf{E}$ and $\mathbf{B}$ are found on shifted spatial grids, as well. Once the fields are known at an initial time, it is computationally straightforward to implement this forward propagation.

Absorbing boundary conditions on the edge of the computational region are generally used to ensure that outward propagating fields are not reflected from the boundaries back into the computational region.

The initial fields that are used depend on the properties that are of interest. Commonly, one would like to determine the local fields within and around a metal nanoparticle when it is illuminated by a plane wave. The initial fields, then, correspond to a plane-wave pulse that originates far from the nanoparticle. The field is propagated over a time much longer than the time needed for the pulse to pass through the nanostructure to the boundary of the computational domain. Frequency-dependent properties can be obtained by repeating the calculation for a series of monochromatic incident fields at different frequencies, or by using a broadband incident pulse and performing a Fourier analysis of the computational results.

The direct result of such a calculation is the near-field distribution around the metal nanoparticle. Far-field characteristics, such as scattering and absorption cross-sections, can be obtained from these near fields through appropriate surface integrals over fields. Writing the total electric field around the nanoparticle as $\mathbf{E} = \mathbf{E}_\mathrm{i} + \mathbf{E}_\mathrm{s}$, where $\mathbf{E}_\mathrm{i}$ is the incident plane wave field and $\mathbf{E}_\mathrm{s}$ is the scattered field, the total Poynting vector is

$$\mathbf{S} = \frac{c}{8\pi}\mathrm{Re}\{\mathbf{E} \times \mathbf{B}^*\} \tag{1.62}$$

$$= \frac{c}{8\pi}\mathrm{Re}\{\mathbf{E}_\mathrm{i} \times \mathbf{B}_\mathrm{i}^*\} + \frac{c}{8\pi}\mathrm{Re}\{\mathbf{E}_\mathrm{s} \times \mathbf{B}_\mathrm{s}^*\} + \frac{c}{8\pi}\mathrm{Re}\{\mathbf{E}_\mathrm{i} \times \mathbf{B}_\mathrm{s}^* + \mathbf{E}_\mathrm{s} \times \mathbf{B}_\mathrm{i}^*\} \tag{1.63}$$

$$\equiv \mathbf{S}_i + \mathbf{S}_s + \mathbf{S}_\mathrm{ext}. \tag{1.64}$$

Here, $\mathbf{S}_\mathrm{i}$ is the energy flux of the incident field, $\mathbf{S}_\mathrm{s}$ is the energy flux of the scattered field, and $\mathbf{S}_\mathrm{ext}$ is the remaining energy flux due to the interference terms. If the nanoparticle is in a nonabsorbing medium, then the energy absorbed by the nanoparticle F_a is the energy flux through any surface Ω that encompasses the nanoparticle, as illustrated in Figure 1.10:

$$F_a = -\int_\Omega \mathbf{S} \cdot \mathbf{n}\, d\Omega, \tag{1.65}$$

where $\mathbf{n}$ is the outward surface normal. Similarly, the outward energy flow through Ω due to scattering is

$$F_s = \int_\Omega \mathbf{S}_s \cdot \mathbf{n}\, d\Omega \tag{1.66}$$

and the inward energy flow from the interference terms is

$$F_\mathrm{ext} = -\int_\Omega \mathbf{S}_\mathrm{ext} \cdot \mathbf{n}\, d\Omega. \tag{1.67}$$

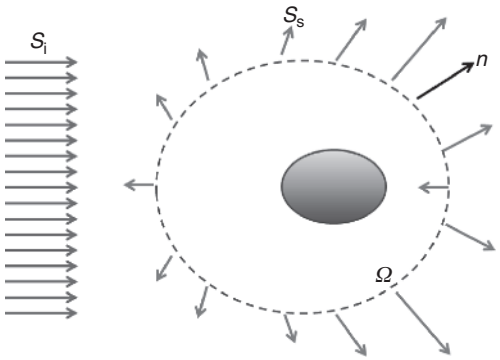

FIGURE 1.10 Energy flux $\mathbf{S}_i$ of an incident field crossing an surface Ω, with the resulting flux $\mathbf{S}_s$ that scatters from a metal nanoparticle. A surface normal **n** is shown.

The energy flow of the incident plane wave across Ω vanishes. From Equation 1.64, energy conservation gives

$$F_{ext} = F_{abs} + F_s. \tag{1.68}$$

F_{ext} equals the energy lost from the incident beam by absorption into the nanoparticle and scattering out of the incident plane wave; this combination of absorption and scattering is known as extinction. Cross sections $\sigma_{ext,abs,scat}$ for extinction, absorption and scattering are defined by normalizing the respective energy flow $F_{ext,a,s}$ by the incident intensity.

Calculating a cross-section is thus a matter of calculating a time-averaged Poynting vector, integrated over an appropriate surface Ω. For calculation of σ_{abs}, the total Poyting vector is integrated, including the contribution from the incident field. In this case, the incident field passes through Ω, as illustrated in Figure 1.10. For calculation of σ_s, only the scattered field is wanted, so the known incident field must be excluded.

Plane waves are not the only incident fields that can be treated using the FDTD method. Indeed, it is straightforward to implement an arbitrary incident field, or to include local sources of radiation. Including dipole radiation sources makes it possible, for example, to calculate how radiation from a localized emitter is modified by the presence of the metal nanoparticle (see Section 6.1.3). Similarly, it is straightforward to calculate any other physical quantity of interest that depends on the electromagnetic field distribution, such as optical forces (see Section 7.5). It is also relatively straightforward to incorporate more complicated material responses, including optical nonlinearities (see Chapter 5).

However, the FDTD method is a volume approach, which means that the computational resources required increase rapidly with the size of the system to be studied, including both the particles and the regions where fields are determined. Calculating fields can become computationally expensive if far-field properties are needed.

Moreover, systems with multiple length scales are difficult to study with the uniform grids typically employed. In addition, FDTD can have problems treating media with high dielectric contrast and damping, such as metals. Despite these difficulties, the FDTD method is one of the most widely used and successful numerical approaches. Its popularity is tied to its intuitive simplicity, the explicit calculation of fields, the calculation of fields in the time domain that allows for revealing animations, the ready availability of commercial packages, and the possibility of efficient parallelization on high-performance computing clusters.

1.3.2 Discrete Dipole Approximation

Real dielectric materials are made up of polarizable atoms arranged in a regular crystal structure or in an amorphous assembly. The polarizability of the solid arises from the polarizabilities of each of the atoms, interacting with one another. Likewise, if individual nanoparticles are arranged in some specific configuration, the polarizations of all of the particles will interact with one another to give an overall, collective response for the entire arrangement. (This coupling is considered in detail in Chapter 4.) Conversely, if a complex nanostructure is decomposed into a number of simpler components, then the response of the entire nanostructure can be calculated from the known response of the individual building blocks. This is the approach taken by the DDA. Each structure to be simulated is represented by a grid of discrete, mutually interacting dipoles, each having the polarizability of the material volume element that it represents. Each dipole is polarized by the external driving fields plus the fields of all the other dipoles.

In the frequency domain, the local field at dipole i is

$$\mathbf{E}_i^{\text{loc}}(\omega) = \mathbf{E}_i(\omega) + \sum_{j \neq i} \mathbf{G}_{ij}(\omega)\alpha_j(\omega)\mathbf{E}_j^{\text{loc}}(\omega), \tag{1.69}$$

where $\mathbf{E}_i$ is the driving field at the location of dipole i, α_j is the polarizability of dipole j, and $\mathbf{G}_{ij}$ is the free-space Green's tensor which propagates a field from j to i. Determining the response of the structure thus requires, first, self-consistently determining the local field at each dipole. Typically, this is done by writing Equation 1.69 as a matrix equation for all of the dipoles in the array and inverting the large matrix that results. Once the local fields at each dipole are determined, the field equation can be used to find the electric field at any point outside the dipole array.

The DDA is intuitively compelling and, like the FDTD method, straightforward to apply to arbitrary structures. Although the DDA is also a volume approach, only the structures must be discretized, and fields outside the structures are determined from the fields generated by the dipoles. Multiple length scales, though, can still be a problem, with accurate calculations of fields near the surface of a nanostructure requiring high densities of dipoles.

The DDA is similar in spirit to Green's function approaches, which therefore have similar advantages and limitations. In these approaches, the material structures

are treated as perturbations to the surrounding media. The polarization due to these perturbations produces fields, which are determined using the Green's function for free propagation in the surrounding medium away from a point source.

1.3.3 Boundary-Element Methods

The computational resources required by the FDTD method and the DDA method both scale with the volume of the simulation. In contrast, the MMP and BEM both scale with the area of interfaces in the system and can, in principle, be more computationally efficient. In both cases, the boundary conditions for Maxwell's equations at the interfaces are used to establish a set of equations for each surface point, and the solution to these equations determines the field distribution in space. In practice, these surface equations are solved on a grid of points on the interfaces between different material regions. In both cases, the equations are solved in the frequency domain.

In the BEM, effective charges and currents at each point on the surface grids are used to solve the boundary conditions for an incident, driving field. In particular, the fields at a given surface point can be written in terms of the surface charges and currents at the other surface points, in a manner analogous to the DDA. As in the DDA, a large matrix equation must be inverted in order to self-consistently determine these surface charges and currents. The fields can then be found throughout space using a Green's-function approach, as in the DDA, to propagate the fields away from the surface charges and currents.

Because the BEM determines effective surface charge densities, it is easy to build up an intuitive physical picture for the plasmon excitations. The BEM easily handles variable grids, allowing surface regions where fields are highly localized to be treated with a high-density grid, without expending the same computational effort elsewhere where requirements for spatial resolution are less demanding. The BEM is well suited for problems where the surfaces are smooth and can easily be defined, and is more difficult to use for complex surfaces or surfaces with sharp contours and edges.

1.3.4 Multiple Multipole Methods

In the MMP, fields are represented by multipolar expansions, similar to the expansion used in Mie theory, but for more complex geometries than spheres. Often, several multipolar expansions about different points outside of a region are used to define the field inside a region, and different spatial regions are described using different expansions. The multipole coefficients are determined by solving the boundary conditions for Maxwell's equations at a grid of points on the surfaces separating different regions. This approach can best be applied when these surfaces are easily defined, as for the BEM. For symmetrical structures, the placement and the form of the multipole expansions are clear, and a limited number of multipoles can describe an entire system. In this case, the expansions provide an intuitive picture of the fields in terms of the excited multipoles. For more complicated structures, the number, placement and

form of the multipoles are less obvious. When multiple expansion points are used, the expansion can become overcomplete. There may be many reasonable choices, making the choice arbitrary, more difficult to reliably control, and less physically motivated.

1.4 A MODEL SYSTEM: GOLD NANORODS

A principal goal of modeling the optical properties of metal nanoparticles is to develop a general understanding of the properties of plasmon resonances in the particles and the key factors that control those resonances. Gold nanorods provide a good model system for developing this understanding because they have been studied theoretically in detail [26–39] because their relatively simple geometry can be readily manipulated to reveal rich behavior, and because they have been widely studied experimentally.

In this section, we describe the results of rigorous numerical simulations of gold nanorods in the fully retarded limit. The fields are found numerically and the particle response is determined from these fields. The nanorods display strong plasmon resonances around particular frequencies, although the resonances are significantly broadened by the material damping inherent in gold. We examine the properties of these resonances and how they are determined by nanoparticle size and shape, the polarization of the excitation, and the nanoparticle environment.

1.4.1 Near-Field Response

In order to gain insight into the plasmonic response of gold nanorods, we will examine the results of numerical simulations using the boundary-element method [26, 40]. In the simulations, the nanorods are modeled as circular cylinders of length L_{rod} and radius R, with hemispherical end caps and total length $L_{\text{tot}} = L_{\text{rod}} + 2R$.

The immediate result of the simulation is the near-field distribution; that is, the electromagnetic fields within the nanoscale environment of the particle. Typical distributions of the magnitude of the electric field are shown in Figure 1.11(a-b) for dipolar resonances of the nanorods. These resonances have been excited by an incident plane wave polarized along the long axis of the rods. A key property of the near field is that it is significantly enhanced near the ends of the nanorods, as compared with the incident field. The longitudinal resonance shifts to lower frequency with increasing rod length because the restoring force due to the charge separation weakens as the charge is separated over longer distances.

Light polarized perpendicular to the rod axis, by contrast, excites transverse resonances, which shift slightly to higher frequencies with increasing rod length. For the lowest-order transverse resonance, near-field enhancement occurs on the side of the nanorod.

As the nanorod length increases, higher order resonances appear. For smaller R, the first additional resonances to appear are higher order longitudinal modes. For

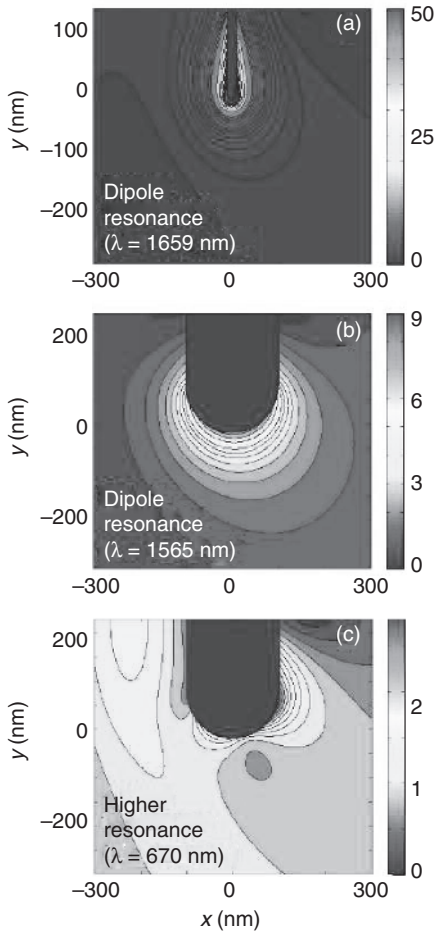

FIGURE 1.11 Electric-field magnitudes for dipolar resonances of gold nanorods with lengths $L_{\text{rod}} = 300$ nm and radii (a) $R = 10$ nm and (b) $R = 100$ nm. A higher order resonance for $R = 100$ nm is shown in (c). Fields are calculated using the boundary-element method for excitation by a plane wave polarized along the long axis of the rods. The magnitude of the plotted field is normalized by the magnitude of the incident plane wave. From Reference [13]. Copyright 2008 Wiley-VCH Verlag GmbH & Co. KGaA, Weinheim.

thicker nanorods, on the other hand, the first higher order resonance to appear can have a transverse nature, with weak near-field response at the end of the rod, as illustrated in Figure 1.11(c). That a transverse mode can be driven by a longitudinal polarization is a signature of the onset of retardation effects: the surface charges on opposite sides of the nanorod are driven by local incident fields with different phases.

Figure 1.12 examines the enhanced near field at the end of a Au nanorod around a dipolar resonance. The real component of the field, which is in phase with the external driving field, shows a dispersive dipolar response around the resonance wavelength

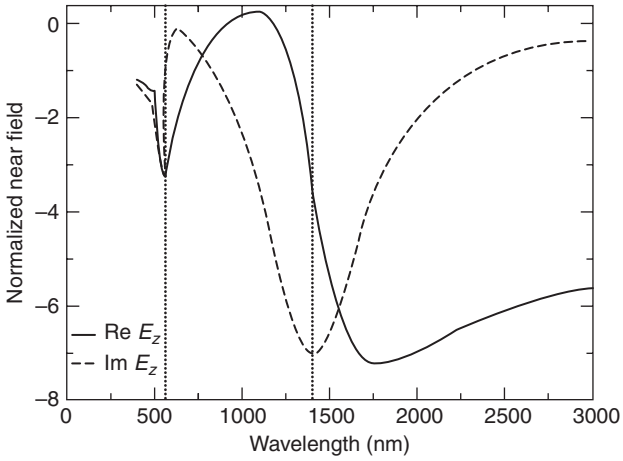

FIGURE 1.12 Real and imaginary components of the electric field 1 nm from the end of a gold nanorod as a function of the wavelength of the driving field. The rod has a length $L_{\text{tot}} = 500$ nm and radius $R = 100$ nm, resulting in a dipolar resonance near 1400 nm. The near field is normalized by the incident driving field, which is polarized along the long axis of the rod.

of approximately 1400 nm. The imaginary component of the field, which is out of phase with the driving field, shows a broadened, dissipative response around the same resonance wavelength.

However, this wavelength-dependent response applies only at a particular point next to the nanorod. In general, the wavelength at which the near field is a maximum depends strongly on the location along the rod where the near field is monitored. The resonance shifts to shorter wavelengths as the measurement position is moved along the rod from the end to the center, while remaining a fixed distance away from the surface, as shown in Figure 1.13. Near the center of the rod, in fact, the dipolar resonance disappears and higher order resonances at shorter wavelengths are more prominent. This variation of the resonance along the rod axis is of great importance for any application that exploits the plasmon resonance to modify the response of attached molecules or other nanostructures (see Section 6.1.3).

1.4.2 Far-Field Response

We have seen that the near-field response of a gold nanorod displays complex resonance behavior that depends on the polarization of the driving field and on the position close to the rod where the near field is monitored. The near-field response also differs significantly from the far-field response. The differences can be important, and must be accounted for when interpreting data or designing structures to respond at desired wavelengths. These differences are illustrated in Figure 1.14.

The far-field scattering for wavelengths shorter than 500 nm is due to the bulk response of gold, and a corresponding response is not seen in the near field. The longest-wavelength peaks in the scattering or near-field amplitude corresponds to

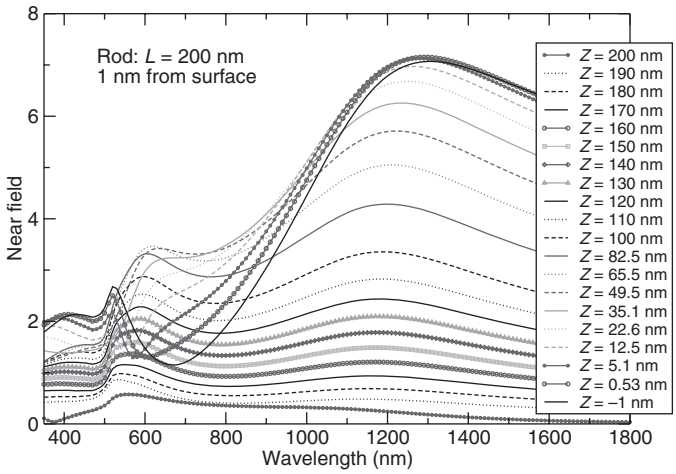

FIGURE 1.13 Position dependence of the near-field response of a gold nanorod with a length $L_{\text{tot}} = 400$ nm and radius $R = 100$ nm. The positions shown are 1 nm from the rod surface. Z labels the distance along the rod axis from the end of the rod ($Z = 200$ nm is the postion above the middle of the rod, and $Z = -1$ nm is the point 1 nm outside the end of the rod.) The near-field magnitude is normalized by the magnitude of the incident driving field, which is is polarized along the rod axis.

the dipole resonances. The wavelengths of these peaks increase approximately linearly with increasing length of the rod, except when the length is comparable to the lateral dimension $2R$ and end effects are dominant, as shown in Figure 1.15. For small R, dipole resonance wavelengths extracted from the far-field and near-field response are nearly identical. As R increases, the near-field resonance is shifted to significantly longer wavelengths than the far-field resonances. For example, for $R = 100$ nm, the shift is about 200 nm, comparable to the linewidth of the resonance. This shift is a signature of the onset of retardation effects, which become important for rod diameters on the order of one fifth of a wavelength. The difference between the two peak wavelengths demonstrates that, although it may be possible to define a plasmon resonance wavelength for the nanorods, the wavelength does not necessarily correspond to the wavelength at which the response of the nanoparticles is a maximum. Rather, the effective resonance wavelength depends on which response is of interest.

The details of the nanoparticle geometry also play an important role in determining plasmon resonances. This is illustrated in Figure 1.16, which compares scattering from nanorods to scattering from ellipsoidal nanoparticles with the same aspect ratios, diameters, and lengths. (In this example, we consider nanoparticles in an environment with a large dielectric constant.) Despite the similar geometries, significant differences are seen. In particular, the nanorods support multiple higher order longitudinal resonances, whereas the ellipsoids support only a single longitudinal mode for all of the lengths considered. Similarly, the ellipsoids support only a single transverse mode, whereas the nanorods support two transverse modes. The geometry of the

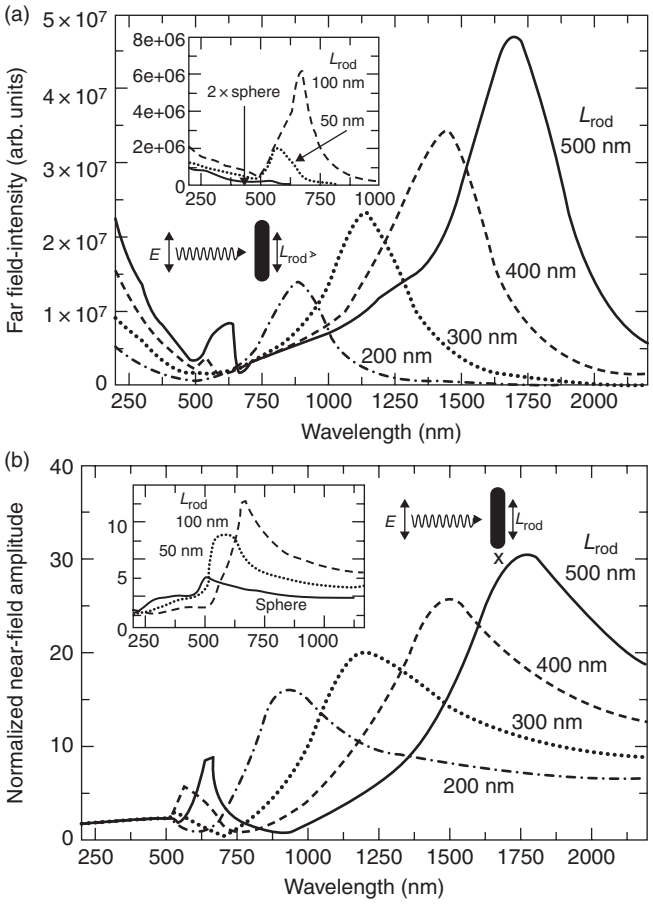

FIGURE 1.14 (a) Far-field scattering intensity as a function of wavelength for an incident plane wave polarized parallel to a gold nanorod with a radius $R = 40$ nm. (b) Normalized near-field amplitude 1 nm from the nanorod end. From Reference [26].

ellipsoid, with a diameter that increases continuously from its end to its middle, means that it acts more like a sphere than a nanorod does.

1.4.3 Optical Antennas and Effective Wavelength

We have seen, in Figure 1.15, that the resonance wavelength of dipolar plasmons in nanorods, λ_{res}, scales linearly with the total nanorod length, L_{tot}, at least over a certain range of L_{tot}. This scaling has prompted many researchers to draw an analogy between this dipole resonance and the half-wave dipole antennas that are commonly used at microwave and radio-wave frequencies [26, 41–46]. At microwave and radio-wave frequencies, metals are nearly perfect conductors, and the dipolar resonance occurs when the length of the antenna is a half-wavelength. It is tempting to assume that the

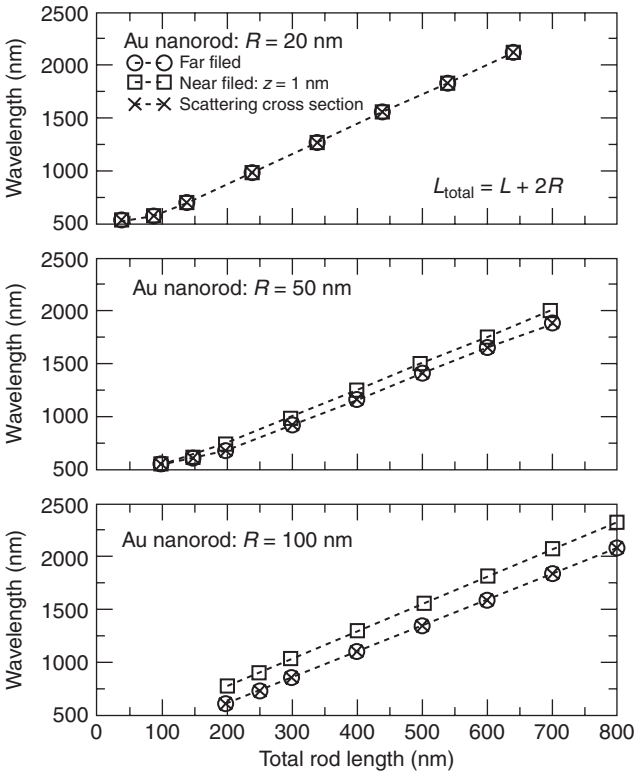

FIGURE 1.15 Dependence of the dipolar resonance wavelength on nanorod length for nanorod radii $R = 20$, 50, and 100 nm. Resonance wavelengths are shown for the calculated far-field spectrum in the forward direction, the far-field scattering cross-section, and the normalized near-field amplitude. From Reference [40].

same will apply for optical resonances in metal nanorods, and the dipolar mode of these "nanoantennas" is often referred to as the $\lambda/2$ mode. However, simulations show that this simple assignment does not apply [26, 45]. Rather, the linear dependence of the dipole resonance on L_{tot} varies substantially with R, as shown in Figure 1.15 and, for a larger range of R, in Figure 1.17.

For a half-wavelength antenna made from a perfect conductor, the resonance wavelength and rod length should be related according to $L_{\text{tot}} = L_o + S\lambda_{\text{res}}$, with a slope $S = 1/2$. For small R, nanoantennas have $S \sim 0.2$ [40], meaning that the nanorod length is much less than half a wavelength. As R increases, the slope S increases monotonically, approaching 0.4 for large R. This means that nanoantennas remain far from being $\lambda/2$ antennas, even for micrometer-size structures.

This deviation from the perfect-conductor case is partially due to the finite skin depth of gold. For microwave and radio-wave antennas, the skin depth is negligible compared with the dimensions of the antenna. The response of the antennas is thus determined by currents on the surfaces of the conductors. At optical wavelengths, on

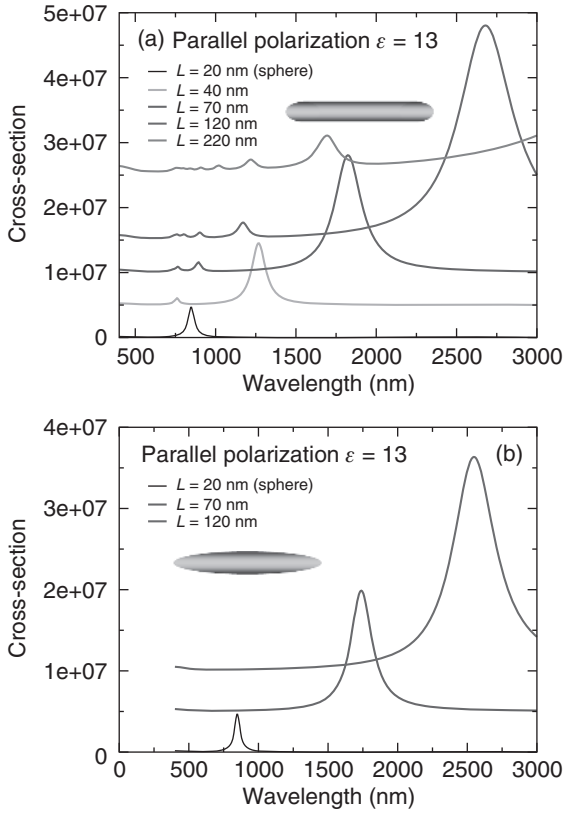

FIGURE 1.16 Scattering cross-sections for gold nanoparticles embedded in a medium with a large dielectric constant ϵ: (a) nanorods, (b) ellipsoidal nanoparticles. The nanoparticle radii are $R = 10$ nm. The particles are excited by a plane wave polarized along their long axis.

the other hand, the skin depth of 20–30 nm in gold or silver is comparable to the total size of the nanoantenna [45]. The response is thus determined by charge oscillations, or volume currents, throughout the entire nanoparticle. Internal losses slow down these oscillations and increase the resonant wavelength.

The fact that the resonance wavelength depends on nanorod radius, and not just on length, is clear in the quasistatic limit. In the quasistatic limit, the resonance wavelength depends only on aspect ratio, which will be different for nanorods with identical L_{tot} but different R. The quasistatic model is simple and intuitively compelling, so many of the theoretical studies of nanorods have considered only the dependence of plasmon resonances on aspect ratio, ignoring any explicit dependence on L_{tot} or R. It is, therefore, important to test the applicability of this model, to see whether it holds any better than the half-wave-antenna model. Figure 1.18 shows the results of full electromagnetic calculations. There is no region where the plasmon resonance wavelength depends only on the aspect ratio, except for the very smallest, nearly spherical nanorods. This shows that the requirement that the nanoparticle

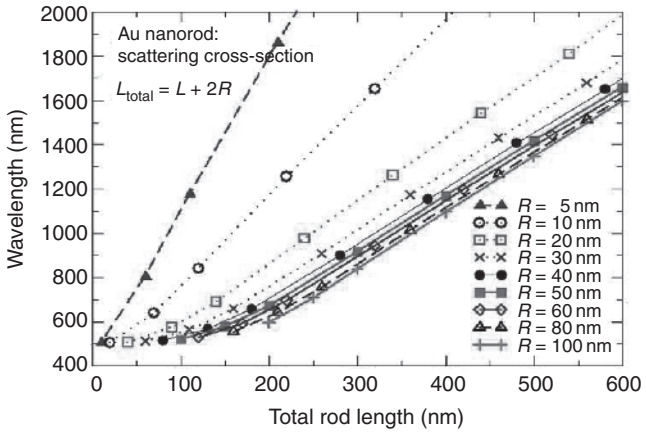

FIGURE 1.17 Dependence of the longitudinal-dipole resonance wavelength in gold nanorods on the nanorod length for different radii, R. The resonance wavelength shown is extracted from the far-field scattering spectrum.

dimensions be much less than the wavelength is very stringent, and, outside of this highly restricted range, the quasistatic approximation is limited.

1.4.4 Effect of the Environment

We have seen that the details of nanoparticle size and shape play important roles in determining the position and strength of plasmon resonances. The environment of the nanoparticle also plays a key role. So far, we have mainly considered nanoparticles

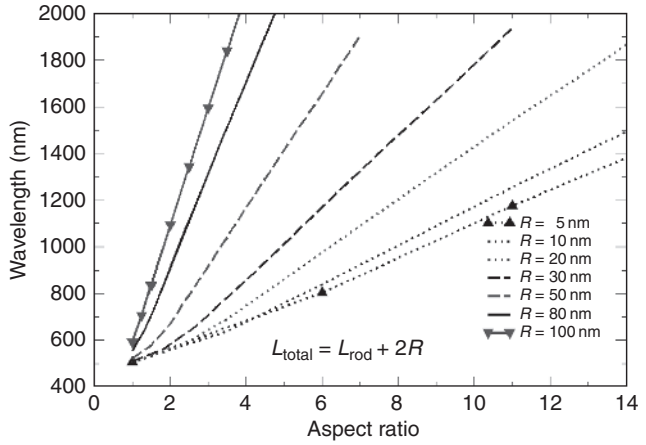

FIGURE 1.18 The dependence of the longitudinal-dipole resonance wavelength in gold nanorods on the aspect ratio of the rods, $L_{tot}/(2R)$, where L_{tot} is the rod length and R is the radius. The resonance wavelength shown is extracted from the far-field scattering spectrum. From Reference [40].

in air, with $\epsilon_{out} = 1$. In most experiments, the nanoparticles are either suspended in a fluid, embedded in a transparent dielectric, or deposited on a substrate. These surroundings are commonly treated theoretically by assuming the nanoparticle is surrounding by a homogeneous material with a real, wavelength-independent $\epsilon_{out} > 1$. We have already seen, in Section 1.2.1, that increasing ϵ_{out} shifts the plasmon resonance of spheres in the quasistatic limit to lower frequency. The shift occurs because the dielectric environment screens the local fields around the nanoparticle, reducing the restoring forces that determine the charge oscillation.

Similar frequency shifts occur for all plasmonic metal nanoparticles, and can be used as a means of sensing changes in the dielectric environment (see Section 7.1). We illustrate these effects for longitudinal plasmon resonances in gold nanorods in Figure 1.19. To observe strong differences, we compare a nanorod in air with a nanorod in an environment with very high dielectric constant $\epsilon_{out} = 13$. Such a high-dielectric constant would correspond to a nanorod embedded in a transparent semiconductor. The nanorod in air exhibits a strong dipolar resonance and much weaker higher order response. In the high-dielectric environment, all of the modes are strongly shifted to longer wavelengths. The higher order modes, which originally occur at wavelengths where gold is highly lossy, are shifted to a spectral region with less loss and therefore become much more distinct. At the same time, the screening provided by the high-dielectric environment reduces the near fields at the ends of the rods.

The influence of the dielectric environment on transverse modes can be even more dramatic, as shown in Figure 1.20. In air, the transverse mode is weak, with a scattering cross-section several orders of magnitude lower than that of the longitudinal mode. Only a single transverse resonance is visible, which shifts slightly to shorter wavelengths as the length of the rod increases. As the dielectric constant of the environment is increased, the transverse mode splits into two. The pair of peaks is strongly shifted toward longer wavelengths, and the scattering cross-section becomes nearly as large as that of the longitudinal modes. Furthermore, strong near fields develop at the ends of the rod.

1.5 SIZE-DEPENDENT EFFECTS IN SMALL PARTICLES

In the previous section, we have seen that not only the shape but also the size of gold nanorods influences their plasmon resonances. For particle dimensions larger than the quasistatic limit, the plasmon resonances shift to longer wavelengths as the particle becomes larger. This shift is due to the retardation effects: the phase of the exciting field varies across the particle. As we have seen, this shift occurs even for relatively small particles; that is, the quasistatic limit only applies for particles much smaller than the optical wavelength (i.e., for particle diameters smaller than about 20 nm at optical wavelengths). As the plasmon resonance peak shifts to longer wavelengths, it also broadens, reflecting a reduction in the plasmon lifetime. This occurs primarily because of radiative damping: the dipole moment due to the oscillating charges in the nanoparticle increases, so that the radiative decay rate of the dipole also increases.

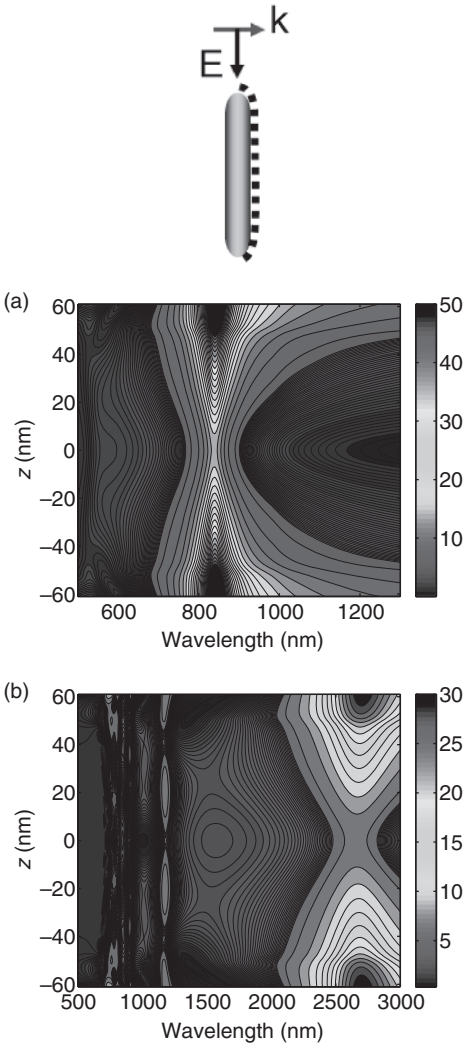

FIGURE 1.19 Wavelength dependence of the near-field enhancement 1 nm away from the surface of a gold nanorod with a length $L_{tot} = 120$ nm, for an incident plane wave polarized along the long axis of the rod. z is the near-field position along the axis, as shown in the schematic. (a) Nanorod in air, (b) nanorod in a dielectric with $\epsilon_{out} = 13$.

Radiative damping is proportional to the polarization of the particle, and thus scales approximately with the nanoparticle volume.

Apart from radiative damping, the only processes that contribute to plasmon decay at these size scales are intrinsic losses in the metal. In a semiclassical picture, these are due to the coupling of the oscillating electrons with interband transitions, scattering of the electrons with phonons, and scattering of the electrons with one another [47].

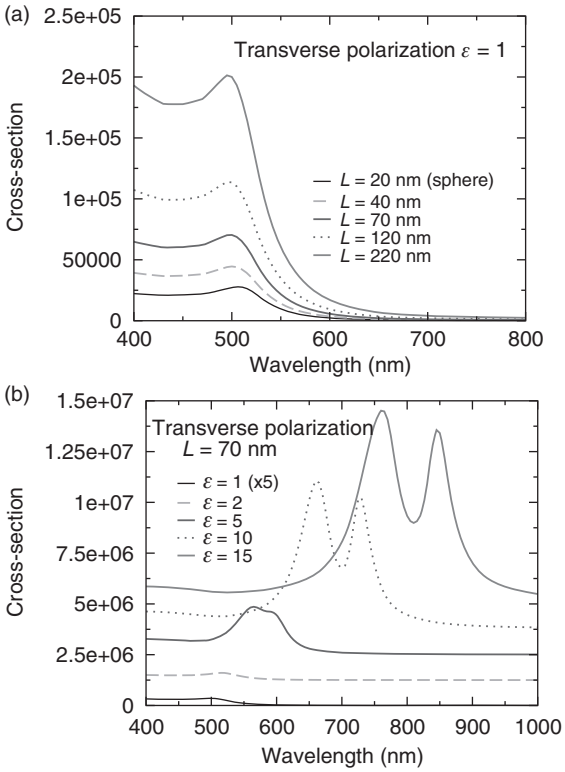

FIGURE 1.20 Scattering cross-section for a gold nanorod with radius $R = 10$ nm excited by a plane wave polarized perpendicular to its long axis. (a) Rods with different lengths in air, (b) rods with length $L = 70$ nm in different dielectric environments.

These scattering rates are well understood from bulk studies of gold, and reproduce well experimentally measured damping rates. For silver and gold at optical and near-infrared frequencies, the damping rates correspond to plasmon lifetimes in the range of 5–50 fs. This intrinsic damping rate depends only on the frequency of the plasmon resonance and on the metal used. The shape and size of the particle affects the damping rate indirectly, by affecting the resonance frequency, but does not have any direct influence on plasmon losses (in the absence of radiative damping).

These properties can all be described quantitatively using the classical electrodynamic methods that we have been using throughout this chapter. Internal losses in the metal are incorporated phenomenologically into the bulk-dielectric function of the metal. Using this dielectric function as an input parameter, Maxwell's equations are solved, applying abrupt boundary conditions at the surfaces of the metal nanoparticle. This approach has been highly successful in explaining the plasmonic properties of metal nanoparticles, but it clearly must have its limitations. The assumption of an abrupt boundary between the metal and the surrounding environment; the treatment of the metal crystal as a continuous, homogeneous material; and the neglect of

quantum-mechanical effects are all good approximations for large particles, but will eventually break down as the particles become smaller and smaller.

In principle, it would be possible to calculate the optical response of small metal nanoparticles using fully quantum-mechanical, *ab initio* calculations. Even the most efficient quantum calculations, though, require computational resources that increase rapidly with the size of the system, and it is not feasible to simulate systems of more than a few hundred atoms. Understanding the optical properties of very small metal nanoparticles, with dimensions below 5 nm, and their deviation from classical predictions, thus requires the development of phenomenological models. In this section, we discuss some of the approaches that have been developed.

1.5.1 Surface Scattering and Nonlocal Effects

Measurements on metal nanoparticles with dimensions less than about 10 nm indicate that the linewidth of the plasmon resonance increases as the particle gets smaller. This broadening cannot be accounted for in classical electrodynamics simulations that describe the nanoparticle response using bulk-dielectric functions. In other words, there appears to be an additional, size-dependent damping mechanism at these sizes that becomes more important for decreasing particle dimensions.

The additional damping has generally been attributed to scattering of electrons at the surfaces of the nanoparticle. This surface scattering has been taken into account phenomenologically by increasing the damping rate in the Drude part of the dielectric function, Equation 1.19 [48, 49]. This model is based on the semiclassical relationship in bulk metals between the mean free path for electron scattering, l, and the energy dissipation rate, γ_l:

$$\gamma_l = \frac{v_\mathrm{F}}{l}\,, \tag{1.70}$$

where v_F is the Fermi velocity of conduction electrons in the metal. For particles with dimensions less than l, the additional scattering of electrons by the surface results in a mean free path that is shorter than the bulk value, l. This reduction in mean free path is taken to be proportional to the mean free path between surface-scattering events, D_eff. For spherical particles, D_eff is simply the diameter of the particle; for nonspherical particles, it is given by $D_\mathrm{eff} = 4V/S$, where V is the particle volume and S is its surface area.

The total dielectric function of the metal is then taken to be

$$\epsilon(\omega) = \epsilon_\mathrm{IB}(\omega) + \epsilon_0(\omega) - \frac{\omega_\mathrm{p}^2}{\omega^2 + i\omega\gamma_\mathrm{s}}\,, \tag{1.71}$$

where $\epsilon_\mathrm{IB}(\omega)$ is the contribution to the dielectric function due to interband transitions, and the total scattering rate γ_s is

$$\gamma = \frac{1}{\tau} + 2\frac{Av_\mathrm{F}}{D_\mathrm{eff}}\,. \tag{1.72}$$

Here, τ is the bulk plasmon lifetime and A is a phenomenological "scattering parameter" on the order of unity. Detailed models can be developed that provide specific values of A, but it is generally taken to be an adjustable parameter when comparing to experiment. Part of the justification for treating A as a fitting parameter is the possibility of "chemical interface damping," or the transfer of energy from the oscillating electrons to the immediate surroundings of the nanoparticle, including capping molecules adsorbed on the metal surface.

The result is that A ends up essentially being a fudge factor that is used to fit measured plasmon linewidths. There has been little consistency in the values of A that have been obtained using this approach, even for nominally identical nanoparticles. The central problem is that the phenomenological model of electron scattering at the surfaces does not represent the physical mechanism by which plasmons lose energy in small particles. In fact, the semiclassical model of electron–electron scattering and electron–phonon scattering in bulk metals is not a true microscopic model of plasmon damping. Fundamentally, plasmons lose their energy by coupling to single-electron excitations in the metal. A single plasmon (that is, a single quantum of the collective electron oscillation) with energy $\hbar\omega$ excites a single electron from an occupied state below the Fermi energy to an unoccupied state, $\hbar\omega$ higher in energy, above the Fermi energy. The rate of this Landau damping in a spherical nanoparticle is inversely proportional to the diameter of the particle, and thus gives qualitatively the same scaling as the surface-scattering model.

Landau damping is ultimately the result of electron–electron interactions that are not included in the Drude model. They can be taken into account by adding electron screening to the Drude model. The simplest approach, known as the random phase approximation, is based on the assumption that an applied potential produces a linear change in electron density [50]. An explicit, albeit complicated, analytical expression for the dielectric function can thereby be obtained, known as the Lindhard dielectric function.

Compared with the Drude model, the Lindhard dielectric function has one key complication: it is explicitly nonlocal. That is, the response at a particular point in space depends not only on the applied field at that point, but also on the applied field at different points. Mathematically, the displacement field $\mathbf{D}(\mathbf{r}, \omega) = \int d\mathbf{r}' \epsilon(\mathbf{r}, \mathbf{r}', \omega)\mathbf{E}(\mathbf{r}', \omega)$. We have already seen something similar in the time domain: even the Drude dielectric function is nonlocal in time, in the sense that the material response at a particular time depends on the field that has been applied at previous times. This temporal dispersion is treated by taking the Fourier transform of the fields in time, and writing the dielectric response as a function of frequency. Similarly, spatial dispersion can be described by taking a Fourier transform in space, and writing the dielectric response as a function of wavenumber q:

$$\mathbf{D}(q, \omega) = \epsilon(q, \omega)\mathbf{E}(q, \omega)\,. \tag{1.73}$$

Here, we have implicitly assumed that the response of the medium is isotropic, so that the response can be written in terms of a single wavenumber. The wavenumber-dependent dielectric function $\epsilon(q, \omega)$ reduces to a local dielectric function in the limit $q \to 0$.

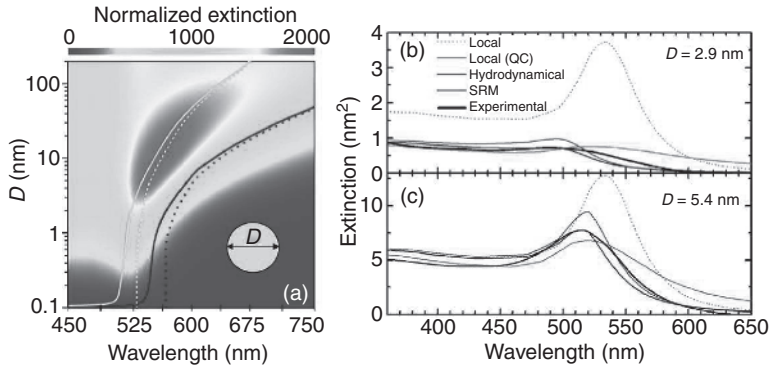

FIGURE 1.21 Effects of nonlocality and retardation on plasmon resonances in a spherical gold nanoparticle in water. (a) The extinction cross-section, normalized by the geometric cross-section, as determined using a nonlocal hydrodynamical model for the electrons in the nanoparticle. The plasmon peak is shown by the solid light curve and the position of the half width by the solid dark curve. The dashed curves show the results calculated using a local dielectric response. D is the particle diameter. (b) Comparison between experiment and theory using different models for the local response: a local response, a local response including surface scattering (QC), the hydrodynamical model, and a nonretarded, nonlocal model, referred to as the SRM. Reprinted with permission from Reference [49]. Copyright (2011) American Chemical Society.

Using a nonlocal dielectric function to calculate optical response is much more involved than using a local-dielectric function. No explicit expressions equivalent to Mie scattering are possible so that numerical calculations are required even for the simplest geometries. Implementation of numerical simulations is also more complicated, and the computation time increases as well. Perhaps most importantly, the nonlocal dielectric function for real metals such as silver and gold are not well known. There are no straightforward methods to measure nonlocal functions, so reliable empirical values are not available.

Moreover, the Lindhard model is not the only nonlocal dielectric function that has been derived theoretically. For example, an alternative approach treats the motion of the conduction electrons hydrodynamically, using a linearized Navier–Stokes equation [49]. Terms added to account for hydrodynamical pressure introduce the nonlocality. The results of calculations using the hydrodynamic model are shown in Figure 1.21 for spherical gold nanoparticles. Also shown are the results of a model known as the specular reflection model (SRM). In this model, the Lindhand dielectric response is used, the quasistatic limit is assumed, and the boundaries between the particles are modeled as boundaries between the corresponding infinite materials, with additional boundary conditions to correct for the simple model. For large particles, there is little difference between the local and nonlocal predictions. However, for particles with diameters less than approximately 10 nm, the nonlocal models predict a shorter resonance wavelength than the local models. This shift can be understood as the effect of the induced screening charge, which penetrates into the particle, reducing the dielectric screening of the restoring force [49]. In addition, the nonlocal models predict increasing damping for smaller particles. This is qualitatively similar to

the increased damping predicted by the surface-scattering model, with the linewidth scaling as $1/D_{\text{eff}}$ in all cases. The detailed spectra, though, are quite different for the different models, and the nonlocal models provide significantly better agreement with experimental results for small particles than the surface-scattering model.

Nonlocal dielectric functions cannot account for all of the effects that occur in small particles. In particular, quantum-mechanical effects may begin to play an important role for particle diameters smaller than a few nanometers. Charges can tunnel off of the metal nanoparticle into the environment, and the wavefunctions of the electrons can extend out from the nanoparticle surface into the environment. The nanoparticle surface then becomes ill-defined, and the dielectric response within the nanoparticle can be modified close to the surface as compared with the rest of the particle. In principle, a quantum mechanical treatment of the metal nanoparticle is needed to account for this tunneling and for the modifications of the dielectric response.

Often, these effects can be treated with the jellium model, which treats the particles as consisting of a uniform density of positive background charge, to represent the ionic cores, and a sea of conduction electrons [51, 52, 53]. The plasmonic excitations of the electron sea can be found using density functional techniques, for example, to explicitly determine the leakage of the electrons out of the particle and to account for any spatial dependence in the dielectric response. For simple, symmetric structures analytic techniques can also be applied. The jellium model again predicts plasmon damping that scales as $1/D_{\text{eff}}$, although with a different quantitative dependence than the other models considered above.

There is clearly an outstanding need to further develop models that incorporate nonlocal and quantum-mechanical effects, that can readily be implemented computationally, and that are validated by quantitative comparison to experiment. This is an experimental challenge as well as a theoretical challenge. In Section 3.2, we will discuss the difficulties associated with measuring the optical response of very small metal nanoparticles. These optical measurements will need to be accompanied by detailed structural studies of the same nanoparticles because atomic-scale structural details will be important for such small particles. In principle, individual crystal defects, surface facets, and crystal orientation all can have an effect on plasmon resonances. In addition, it will be important to consider the electronic nature of the nanoparticle surfaces [54], something that has been ignored in nearly all theoretical treatments to date.

Nonlocality and quantum-mechanical effects play a role not only when the dimensions of the nanoparticle are small, but also when the nanoparticles are very close to other objects. In particular, the coupling between plasmons in metal nanoparticles cannot be fully described using a local, classical treatment for interparticle spacings less than a few nanometers. We will return to this issue in Section 4.1.3.

1.5.2 From Plasmonic Nanoparticles to Molecular Clusters

The nonlocal and quantum-mechanical effects considered above can be treated as corrections to the classical electrodynamic model for the optical response of metal nanoparticles. The nanoparticles are still considered as being made up of continuous

media, with properties that are derived from the properties of bulk metals. This solid-state picture applies, at least qualitatively, down to very small particles: the collective excitations of particles with as few as 500–1000 conduction electrons still behave very much like classical plasmon resonances [55]. Eventually, though, this picture breaks down completely. As particles get even smaller, the broad dipolar resonance splits into a band of discrete modes, with some having the collective character of the classical surface plasmon and others being more strongly localized in the core of the particle. Eventually, when only a few metal atoms are present, the peaks in the absorption spectrum are due to transitions between discrete, quantum-mechanical states, similar to the transitions in isolated atoms or molecules.

These smallest particles have been the subject of extensive, independent theoretical, and experimental studies for several decades. Because they are, in many ways, more like molecules than like plasmonic metal nanoparticles, they are perhaps best referred to as metal clusters. Extensive measurements on isolated clusters in the gas phase or embedded in solid matrices have shown that clusters of approximately 2-100 gold or silver atoms exhibit molecule-like optical properties [56]. Gas-phase clusters, in particular, take on well-defined geometries determined by thermodynamic minima, which means that their optical properties can be modeled explicitly using quantum-mechanical electronic-structure models. More recently, clusters with precisely defined numbers of metal atoms have been synthesized chemically in solution [57], using methods analogous to the colloidal synthesis of metal nanoparticles described in Section 2.2. Unlike gas-phase clusters, but like colloidal metal nanoparticles, these solution-phase clusters are stabilized by organic ligand molecules. The precise structure of many of these clusters has been determined by X-ray crystallography, again enabling electronic-structure calculations [58].

A major outstanding question is how the molecule-like transitions in these clusters evolve into plasmonic resonances as the number of the atoms increases and the clusters approach the size scale of metal nanoparticles. This length scale remains virtually unexplored because of the great challenges involved, both theoretically and experimentally. Understanding how collective plasmonic effects emerge in this intermediate regime will provide the crucial underpinning necessary to develop models for the response of nanoparticles with small dimensions, and will provide fundamental understanding of the nature of plasmon resonances in general.

REFERENCES

1. A. L. Fetter and J. D. Walecka. *Quantum Theory of Many-Particle Systems*. McGraw-Hill, New York, 1971.
2. D. Bohm and D. Pines. A collective description of electron interactions. I. Magnetic interactions. *Phys. Rev.*, 82:625–634, 1951.
3. D. Bohm and D. Pines. A collective description of electron interactions: IV. Electron interactions in metals. *Phys. Rev.*, 92:626–636, 1953.
4. R. H. Ritchie. Plasma losses by fast electrons in thin films. *Phys. Rev.*, 106:874–881, 1957.

5. J. D. Jackson. *Classical Electrodynamics*. John Wiley, New York, 1962.
6. P. B. Johnson and R. W. Christy. Optical constants of the noble metals. *Phys. Rev. B*, 6:4370–4379, 1972.
7. J. A. Stratton. *Electromagnetic Theory*. McGraw-Hill, New York, 1941.
8. A. Sommerfeld. Ueber die fortpflanzung elektrodynamischer wellen längs eines drahtes. *Ann. Physik. Chemie (Neue Folge)*, 67:233–290, 1899.
9. G. Goubau. Surface waves and their application to transmission lines. *J. Appl. Phys.*, 21:1119–1128, 1950.
10. K. Wang and D. M. Mittleman. Dispersion of surface plasmon polaritons on metal wires in the terahertz frequency range. *Phys. Rev. Lett.*, 96:157401, 2006.
11. G. Schider, J. R. Krenn, A. Hohenau, H. Ditlbacher, A. Leitner, F. R. Aussenegg, W. L. Schaich, I. Puscasu, B. Monacelli, and G. Boreman. Plasmon dispersion relation of Au and Ag nanowires. *Phys. Rev. B*, 68:155427, 2003.
12. C. F. Bohren and D. R. Huffman. *Absorption and Scattering of Light by Small Particles*. Wiley, New York, 1983.
13. M. Pelton, J. Aizpurua, and G. Bryant. Metal-nanoparticle plasmonics. *Laser Photon. Rev.*, 2:136–159, 2008.
14. G. Mie. Beiträge zur optik trüber medien, speziell kolloidaler metallösungen. *Ann. Phys. (Leipzig)*, 330:377–445, 1908.
15. R. Fuchs. Theory of the optical properties of ionic crystal cubes. *Phys. Rev. B*, 11:1732–1740, 1975.
16. L. C. Davis. Electrostatic edge modes of a dielectric wedge. *Phys. Rev. B*, 14:5523–5525, 1976.
17. J. Aizpurua, A. Rivacoba, and S. P. Apell. Electron-energy losses in hemispherical targets. *Phys. Rev. B*, 54:2901–2909, 1996.
18. E. K. Miller. Time domain modelling in electromagnetics. *J. Electromagn. Waves Appl.*, 8:1125–1172, 1994.
19. E. M. Purcell and C. R. Pennypacker. Scattering and absorption of light by non-spherical dielectric grains. *Astrophys. J.*, 186:705–714, 1973.
20. B. T. Draine and P. J. Flatau. Discrete-dipole approximation for scattering calculations. *J. Opt. Soc. Am. A*, 11:1491–1499, 1994.
21. O. J. F. Martin, C. Girard, and A. Dereux. Generalized field propagator for electromagnetic scattering and light confinement. *Phys. Rev. Lett.*, 74:526–529, 1995.
22. C. H. Hafner and R. Ballist. The multiple multipole method (MMP). *Int. J. Comp. Math. Elect. Elect. Eng.*, 2:1–7, 1983.
23. J. B. Pendry and A. MacKinnon. Calculation of photon dispersion relations. *Phys. Rev. Lett.*, 69:2772–2775, 1992.
24. K. M. Leung and Y. F. Liu. Photon band structures: The plane-wave method. *Phys. Rev. B*, 41:10188–10190, 1990.
25. F. J. García de Abajo and A. Howie. Relativistic electron energy loss and electron-induced photon emission in inhomogeneous dielectrics. *Phys. Rev. Lett.*, 80:5180–5183, 1998.

26. J. Aizpurua, Garnett W. Bryant, Lee J. Richter, F. J. García de Abajo, Brian K. Kelley, and T. Mallouk. Optical properties of coupled metallic nanorods for field-enhanced spectroscopy. *Phys. Rev. B*, 71:235420, 2005.

27. S. Link and M. A. El-Sayed. Spectral properties and relaxation dynamics of surface plasmon electronic oscillations in gold and silver nanodots and nanorods. *J. Phys. Chem. B*, 103:8410–8426, 1999.

28. S. Eustis and M. A. El-Sayed. Aspect ratio dependence of the enhanced fluorescence intensity of gold nanorods: Experimental and simulation study. *J. Phys. Chem. B*, 109:16350–16356, 2005.

29. S. Eustis and M. A. El-Sayed. Determination of the aspect ratio statistical distribution of gold nanorods in solution from a theoretical fit of the observed inhomogeneously broadened longitudinal plasmon resonance absorption spectrum. *J. Appl. Phys.*, 100:044324, 2006.

30. K.-S. Lee and M. A. El-Sayed. Dependence of the enhanced optical scattering efficiency relative to that of absorption for gold metal nanorods on aspect ratio, size, end-cap shape, and medium refractive index. *J. Phys. Chem. B*, 109:20331–20338, 2005.

31. P. K. Jain, K.-S. Lee, I. H. El-Sayed, and M. A. El-Sayed. Calculated absorption and scattering properties of gold nanoparticles of different size, shape, and composition: Applications in biological imaging and biomedicine. *J. Phys. Chem. B*, 110:7238–7248, 2006.

32. K.-S. Lee and M. A. El-Sayed. Gold and silver nanoparticles in sensing and imaging: Sensitivity of plasmon response to size, shape, and metal composition. *J. Phys. Chem. B*, 110:19220–19225, 2006.

33. E. Hao and G. C. Schatz. Electromagnetic fields around silver nanoparticles and dimers. *J. Chem. Phys.*, 120:357–366, 2004.

34. E. K. Payne, K. L. Shuford, S. Park, G. C. Schatz, and C. A. Mirkin. Multipole plasmon resonances in gold nanorods. *J. Phys. Chem. B*, 110:2150–2154, 2006.

35. A. Brioude, X. C. Jiang, and M. P. Pileni. Optical properties of gold nanorods: DDA simulations supported by experiments. *J. Phys. Chem. B*, 109:13138–13142, 2005.

36. S. E. Sburlan, L. A. Blanco, and M. Nieto-Vesperinas. Plasmon excitation in sets of nanoscale cylinders and spheres. *Phys. Rev. B*, 73:035403, 2006.

37. S. W. Prescott and P. J. Mulvaney. Gold nanorod extinction spectra. *J. Appl. Phys.*, 99:123504, 2006.

38. C. Noguez. Surface plasmons on metal nanoparticles: The influence of shape and physical environment. *J. Phys. Chem. C*, 111:3806–3819, 2007.

39. B. N. Khlebtsov and N. G. Khlebtsov. Multipole plasmons in metal nanorods: Scaling properties and dependence on particle size, shape, orientation, and dielectric environment. *J. Phys. Chem. C*, 111:11516–115127, 2007.

40. G. W. Bryant, F. J. García de Abajo, and J. Aizpurua. Mapping the plasmon resonances of metallic nanoantennas. *Nano Lett.*, 8:631–636, 2008.

41. P. Mühlschlegel, H.-J. Eisler, O. J. F. Martin, B. Hecht, and D. W. Pohl. Resonant optical antennas. *Science*, 308:1607–1609, 2005.

42. F. Neubrech, T. Kolb, R. Lovrincic, G. Fahsold, A. Pucci, J. Aizpurua, T. W. Cornelius, M. E. Toimil-Molares, R. Neumann, and S. Karim. Resonances of individual metal nanowires in the infrared. *Appl. Phys. Lett.*, 89:253104, 2006.

43. E. Cubukcu, E. A. Kort, K. B. Crozier, and F. Capasso. Plasmonic laser antenna. *Appl. Phys. Lett.*, 89:093120, 2006.
44. T. H. Taminiau, R. J. Moerland, F. B. Segerink, L. Kuipers, and N. F. van Hulst. λ/4 resonance of an optical monopole antenna probed by single molecule fluorescence. *Nano Lett.*, 7:28–33, 2007.
45. L. Novotny. Effective wavelength scaling for optical antennas. *Phys. Rev. Lett.*, 98:266802, 2007.
46. O. L. Muskens, V. Giannini, J. A. Sánchez-Gil, and J. Gómez Rivas. Strong enhancement of the radiative decay rate of emitters by single plasmonic nanoantennas. *Nano Lett.*, 7:2871–2875, 2007.
47. M. Liu, M. Pelton, and P. Guyot-Sionnest. Reduced damping of surface plasmons at low temperatures. *Phys. Rev. B*, 79:035418, 2009.
48. U. Kreibig and C. V. Fragstein. The limitations of electron mean free path in small silver particles. *Z. Phys.*, 224:307–323, 1969.
49. C. David and F. Javier García de Abajo. Spatial nonlocality in the optical response of metal nanoparticles. *J. Phys. Chem.*, 115:19470–19475, 2011.
50. N. W. Ashcroft and N. D. Mermin. *Solid State Physics*. Holt, Rinehart and Winston, New York, 1976.
51. E. Prodan and P. Nordlander. Exchange and correlations effects in small metallic nanoshells. *Chem. Phys. Lett.*, 349:153–160, 2001.
52. E. Prodan, P. Nordlander, and N. J. Halas. Electronic structure and optical properties of gold nanoshells. *Nano Lett.*, 3:1411–1415, 2003.
53. J. Zuloaga, E. Prodan, and P. Nordlander. Quantum description of the plasmon resonances of a nanoparticle dimer. *Nano Lett.*, 9:887–891, 2009.
54. S. Peng, J. M. McMahon, G. C. Schatz, S. K. Gray, and Y. Sun. Reversing the size-dependence of surface plasmon resonances. *Proc. Nat. Acad. Sci. USA*, 107:14530–14534, 2010.
55. E. Townsend and G. W. Bryant. Plasmonic properties of metallic nanoparticles: The effects of size quantization. *Nano Lett.*, 12:429–434, 2012.
56. U. Kriebig and M. Vollmer. *Optical Properties of Metal Clusters*. Springer, Berlin, 1995.
57. R. Jin, Y. Zhu, and H. Qian. Quantum-sized gold nanoclusters: Bridging the gap between organometallics and nanocrystals. *Chem. Eur. J.*, 17:6584–6593, 2011.
58. C. Aikens. Electronic structure of ligand-passivated gold and silver nano clusters. *J. Phys. Chem. Lett.*, 2:99–104, 2010.